Evaluation of Coupled Wind–Wave Model Simulations of Offshore Winds in the Mid-Atlantic Bight Using Lidar-Equipped Buoys

BRIAN J. GAUDET,[a] G. GARCÍA MEDINA,[b] R. KRISHNAMURTHY,[a] W. J. SHAW,[a] L. M. SHERIDAN,[a] Z. YANG,[b,c] R. K. NEWSOM,[a] AND M. PEKOUR[a]

[a] *Pacific Northwest National Laboratory, Richland, Washington*
[b] *Pacific Northwest National Laboratory, Seattle, Washington*
[c] *University of Washington, Seattle, Washington*

(Manuscript received 30 June 2021, in final form 26 January 2022)

ABSTRACT: From 2014 to 2017, two Department of Energy buoys equipped with Doppler lidar were deployed off the U.S. East Coast to provide long-term measurements of hub-height wind speed in the marine environment. We performed simulations of selected cases from the deployment using a 5-km configuration of the Weather Research and Forecasting (WRF) Model, to see if simulated hub-height speeds could produce closer agreement with the observations than existing reanalysis products. For each case we performed two additional simulations: one in which marine surface roughness height was one-way coupled to forecast wave parameters from a stand-alone WaveWatch III (WW3) simulation, and another in which WRF and WW3 were two-way coupled using the Coupled Ocean–Atmosphere–Wave–Sediment–Transport (COAWST) framework. It was found that all the 5-km WRF simulations improved 90-m wind speed statistics for the tropical cyclone case of 8 May 2015 and the cold frontal case of 25 March 2016, but not the nor'easter of 18 January 2016. The impact of wave coupling on buoy-level (4 m) wind speed was modest and case dependent, but when present, the impact was typically seen at 90 m as well, being as large as 10% in stable conditions. One-way wave coupling consistently reduced wind speeds, improving biases for 25 March 2016 but worsening them for 8 May 2015. Two-way wave coupling mitigated these negative biases, improved wave field representation and statistics, and mostly improved 4-m wind field correlation coefficients, at least at the Virginia buoy, largely due to greater self-consistency between wind and wave fields.

SIGNIFICANCE STATEMENT: Using atmospheric models to forecast winds in the environments of offshore wind turbines will be critical in the new energy economy. The models used are imperfect, however, being sometimes too coarse, and may not properly represent the wind field at typical turbine hub heights of 90 m, for which we have limited observations in the marine environment. To help address this gap, two buoys equipped with lidars that measured hub-height winds continuously were deployed off the U.S. East Coast from 2014 to 2017. We used the lidar buoy data to show the benefits of a relatively high-resolution atmospheric model over existing reanalysis products, as well as including both the impacts of waves on winds and vice versa.

KEYWORDS: Atmosphere-ocean interaction; Marine boundary layer; Model evaluation/performance

1. Introduction

Offshore wind energy resources will be a key component of the future economy. Being able to assess and predict the offshore wind resource reliably is thus of the utmost importance. A difficulty with the prediction of offshore wind patterns is the general absence of verifying observations at wind turbine hub heights [typically 90 m above mean sea level (MSL)] (Archer et al. 2017; Karagali et al. 2018; Hasager et al. 2020). Satellite-based measurements from synthetic aperture radars and other instruments provide wind speed measurements near the surface (10 m MSL) that can be extrapolated to hub height, but the temporal frequency of the measurements is too coarse (Doubrawa et al. 2015; Hasager et al. 2015; Badger et al. 2016). To address this deficiency, Pacific Northwest National Laboratory, under U.S. Department of Energy sponsorship deployed two buoys equipped with Doppler lidars off the U.S. East Coast from 2014 to 2017 (Shaw et al. 2020; Newsom et al. 2020; Sheridan et al. 2021), which can provide measurements of the horizontal wind vector at typical offshore hub heights as well as standard meteorological measurements at buoy height (4 m).

Sheridan et al. (2020, 2021) used data from the buoys to perform a multiyear evaluation of the biases in near-surface and hub-height wind speeds for reanalysis products commonly used for offshore wind resource assessment. These products generally have horizontal resolutions ranging from 13 km [the Rapid Refresh (RAP) model; Benjamin et al. (2016)] to about 50 km [The second Modern-Era Retrospective Analysis for Research and Applications (MERRA-2; Gelaro et al. 2017)]. They found that the best skill was generally found in the RAP and the European Centre for Medium-Range Weather Forecasts (ECMWF) Reanalysis v5 (ERA5) (Hersbach et al. 2020) products, but varied depending on atmospheric phenomena. Therefore, high resolution atmospheric modeling is necessary to estimate the wind resource accurately at the scales of interest for wind energy.

One unique aspect of the offshore environment is that the surface roughness height cannot be treated as a constant, as it is a function of the wave state. Historically, marine roughness

Corresponding author: Brian J. Gaudet, brian.gaudet@pnnl.gov

DOI: 10.1175/MWR-D-21-0166.1

height, and by implication wave state, has been parameterized as a function of local wind speed (Charnock 1955). While this may be adequate for local wind-generated waves, the relation at higher wind speeds is not fully established (Fairall et al. 2003; Edson et al. 2013), and the impacts of swell and variability of waves due to propagation direction or water depth are not fully accounted for in the parameterizations. Jiménez and Dudhia (2018) found that existing wind speed parameterizations of roughness height could cause systematic biases in forecasted offshore wind speeds over a year-long forecast period if the increased roughness in shallow coastal waters was not considered. Because of this issue, marine roughness height parameterizations more directly related to physical wave characteristics have been developed (Taylor and Yelland 2001; Oost et al. 2002; Drennan et al. 2005). Taking full advantage of these parameterizations, though, requires an explicit, predictive wave model.

In a model surface layer scheme, the direct impact of increasing the surface roughness height will be an increase in the friction velocity for a given model near-surface wind speed, according to the predictions of Monin–Obukhov similarity theory (Edson and Fairall 1998). Friction velocity represents the loss of momentum from the atmosphere to the surface, and when it increases it is expected in turn to cause a decrease in the near-surface wind speed. This latter process, however, occurs over time and its rate is dependent on other parameters in the model, such as the boundary layer depth, which impacts the magnitude of the momentum flux divergence. Thus, the precise relationship between wave parameters and surface wind speed in atmospheric models is unclear.

One tool for understanding this process better is a coupled wave, ocean, and atmosphere modeling system. The Coupled Ocean–Atmosphere–Wave–Sediment–Transport (COAWST) Modeling System (Warner et al. 2010) developed at Woods Hole Oceanographic Institute can provide additional insights into the interplay between hub-height winds and sea state conditions. Among the atmospheric phenomena whose ocean–wave–atmosphere interactions have been investigated by this system have been tropical cyclones (Olabarrieta et al. 2012; Zambon et al. 2014b; Ren et al. 2016; Zhao and Chan 2017; Zang et al. 2018), strong extratropical development (Olabarrieta et al. 2012; Nelson and He 2012; Renault et al. 2012; Nelson et al. 2014; Zambon et al. 2014a; Ricchi et al. 2017), cold air outbreaks (Carniel et al. 2016; Ricchi et al. 2016), and warm season ocean/land circulations (Alves et al. 2018). In these studies, the behavior of the Weather Regional and Forecasting (WRF) atmospheric model and the Simulating Waves Nearshore (SWAN) wave model have been examined, both separately and when coupled.

The general impact of wave–atmospheric coupling on wind speeds in these studies seems to be case dependent. Wave-based roughness heights seemed to reduce biases in wind speed and significant wave height caused by Charnock relations in many cases (Olabarrieta et al. 2012; Renault et al. 2012; Ricchi et al. 2017), though it had little impact on a cold air outbreak cases (Ricchi et al. 2016), and can make some statistics worse by increasing variability (Zambon et al. 2014b). Among different wave roughness parameterizations, Zambon et al. (2014b) found that of Taylor and Yelland (2001) performed better for Superstorm Sandy than those of Oost et al. (2002) and Drennan et al. (2005), while other studies found the performance of Oost et al. (2002) seemed to be superior (Olabarrieta et al. 2012; Carniel et al. 2016).

In this study, we use data obtained from the lidar buoys to verify the skill of in-house model simulations of cases from the East Coast buoy deployment. Our simulations are performed at higher resolution than the reanalyses examined in Sheridan et al. (2021). Cases were chosen where the reanalyses exhibited poor performance compared to offshore lidar-based measurements, and include a number of examples that were previously investigated by COAWST as mentioned above; namely, a tropical cyclone case (8 May 2015), a strong extratropical case (18 January 2016), and a cold frontal case (25 March 2016). We further use the COAWST modeling system to determine the impact of various degrees of wave–atmosphere coupling to the wind speed forecasts of the model configuration. Unlike previous studies of wave–atmosphere coupling with COAWST, we use an implementation of the WaveWatch III (WW3) model based on a configuration previously used at PNNL for an extended simulation of the East Coast deployment period (García Medina et al. 2020). These model results will be used as boundary conditions for the reimplementation of the shelf scale wave model used in the present study. After background on the lidar buoys and models are presented in section 2, section 3 will describe the setup of the model experiments. Section 4 will present model fields and statistics from all three cases, followed by discussion and conclusions in section 5.

2. Background

a. U.S. Department of Energy lidar buoys

The U.S. Department of Energy (DOE) coordinated with Pacific Northwest National Laboratory to deploy two buoys with Doppler lidars to measure the offshore wind resource off the coast of New Jersey and Virginia (Fig. 1). A Vindicator III Doppler lidar was initially installed on the buoys, which is designed to provide profiles of horizontal wind vector from approximately 40–200 m above mean sea level (MSL) with a vertical resolution of 40 m. During the Experimental Planetary Boundary Layer Instrument Assessment (XPIA) validation campaign (Lundquist et al. 2017), it was observed that the Vindicator III lidars have the lowest wind speed bias at 90 m AGL (<0.5 m s^{-1}). More details about the Vindicator III lidar performance during the above deployments can be found in Newsom (2016). In addition to the wind profiles from the lidars, the buoys collected near-surface measurements of wind speed and direction (4 m MSL), air temperature, relative humidity, barometric pressure, and solar irradiance. Oceanographic variables measured include the two-dimensional wave spectrum, water temperature and conductivity, and ocean current vectors to a depth of 90 m. The New Jersey (NJ) deployment (near Atlantic City) was approximately 5 km from the coast at a water

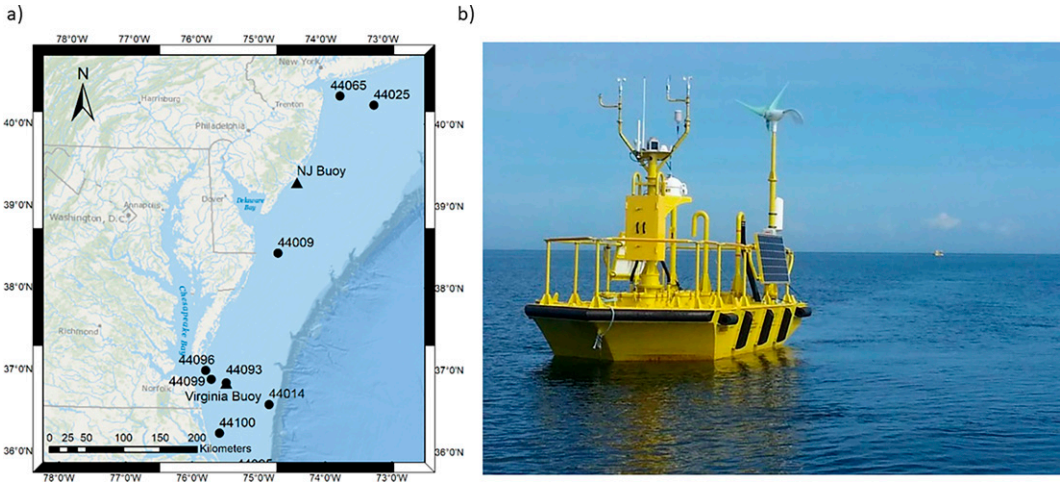

FIG. 1. (a) Location of the two lidar buoys deployed along the East Coast in (triangles) along with long-term buoy monitoring stations (circles); (b) one of the two AXYS WindSentinel buoys operated by PNNL for DOE.

depth of 15 m from 6 November 2015 to 7 February 2017. The Virginia (VA) deployment was approximately 40 km from the coast at a water depth of 26 m from 11 December 2014 to 31 May 2016. Further details about the buoy signal processing, instrument details and general analysis can be found in Shaw et al. (2020).

b. *Modeling systems*

1) COAWST MODELING SYSTEM

The COAWST modeling system is comprised of a set of components for modeling different aspects of the coastal environment (Warner et al. 2010). Specifically, the atmosphere is represented with the WRF model. Wave evolution was originally predicted with the SWAN model, but now, as in this study, can alternatively be predicted with the WW3 model. Although not considered here, the ocean model is the Regional Oceanic Modeling System (ROMS), and a sediment transport model [Community Sediment Transport Modeling System (CSTMS)] is also available.

Within COAWST the different components interact with each other using the Model Coupling Toolkit (MCT), and a customized version of the Spherical Coordinate Remapping Interpolation Package (SCRIP; Jones 1998) is used to conservatively remap fields between the WRF and WW3 grid cells. This does not constrain all models to run on the same mesh allowing optimal configurations for each model.

COAWST has the flexibility to allow different degrees of coupling within the system. Only individual components may be run, or only a pair of components can be run as a two-way coupled system, or all components may be run and interact. In two-way atmospheric/wave coupling, WRF provides wind speed to WW3, while WW3 provides significant wave height and mean wavelength to WRF.

This study will focus only on wave–atmospheric interactions, therefore the WRF and WW3 model components are described in sections below.

2) WRF

We use version 4.0.3 of WRF (Skamarock et al. 2019). This has been a state-of-the-science atmospheric modeling system for the last couple of decades, with both research and forecast applications; for example, WRF is the underlying model used for the RAP (Benjamin et al. 2016) short-term analysis and forecast system that was examined by Sheridan et al. (2021). WRF can be run with multiple nests at grid spacing from subkilometer to hundreds of kilometers, either with or without data assimilation during the simulation. Multiple options for parameterizing boundary layer turbulence, land and ocean surface processes, and other physical processes are available. More details on our particular configuration will be provided in the experimental design section.

3) WW3

Surface gravity waves are modeled with WW3 v5.16 (The WAVEWATCH III Development Group 2016). WW3 is a third-generation, phase-averaged model that solves the wave action balance equation as a function of latitude, longitude, time, wavenumber, and wave direction. The group velocity determines the propagation of wave energy and is solved in WW3 following the linear dispersion relation. More details on our particular configuration can be found in section 3, and more description of the WW3 implementation can be found in Shaw et al. (2020) and García Medina et al. (2020).

3. Experimental design

Our goal is to test the importance of higher-resolution numerical modeling and the inclusion of different degrees of atmospheric/wave coupling for the prediction of offshore 90-m wind speeds, focusing on cases during the buoy deployment for which existing atmospheric analysis products had large errors. Existing analysis products tend to have horizontal grid

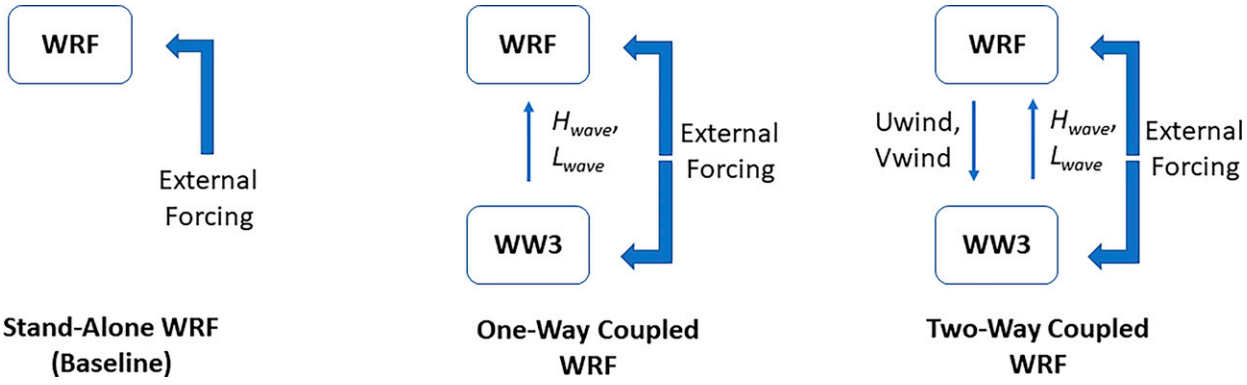

FIG. 2. Schematic showing interactions between WRF and WW3 in simulation experiments.

spacing of 10–50 km (Sheridan et al. 2021), so we chose 5 km as a target for our in-house WRF simulations. For case selection we leveraged the evaluation of multiple atmospheric analyses across the entire buoy deployment period that was performed by Sheridan et al. (2021). We similarly use the deployment data, both at buoy height (~4 m MSL) and lidar-retrieved (~90 m MSL), for the evaluation.

Our simulations were multiday to encompass the weather phenomena of interest. For each case we performed WRF simulations in the following wave-coupling modes: 1) stand-alone WRF with no wave input; 2) one-way coupled WRF, where wave output from a stand-alone WW3 simulation was read into WRF and influences the wind field; and 3) two-way coupled WRF/WW3, where WRF and WW3 are run concurrently within the COAWST framework and interact freely (Fig. 2). For subsequent analysis, a one-way coupled WW3 simulation, with waves driven by stand-alone WRF, was also performed. More information on these modes follows.

a. *Stand-alone WW3*

To simulate waves in the mid-Atlantic Bight, a WW3 model with 2-km grid spacing extending from North Carolina to the northeastern corner of Long Island, New York, was developed based on the configuration used in García Medina et al. (2020). The offshore boundary was extended to at least 200 km from shore, which extends beyond the shelf break, in order to capture the wave transformations as they enter intermediate waters. The model domain is shown in Fig. 3a. Wind forcing for the stand-alone simulations comes from the Climate Forecast System version 2 (CFSv2; Saha et al. 2010; Saha et al. 2014). The CFSv2 is an analysis system with intermittent data assimilation that uses forecasts of fully coupled atmosphere/land/ocean models in the assimilation step, thus

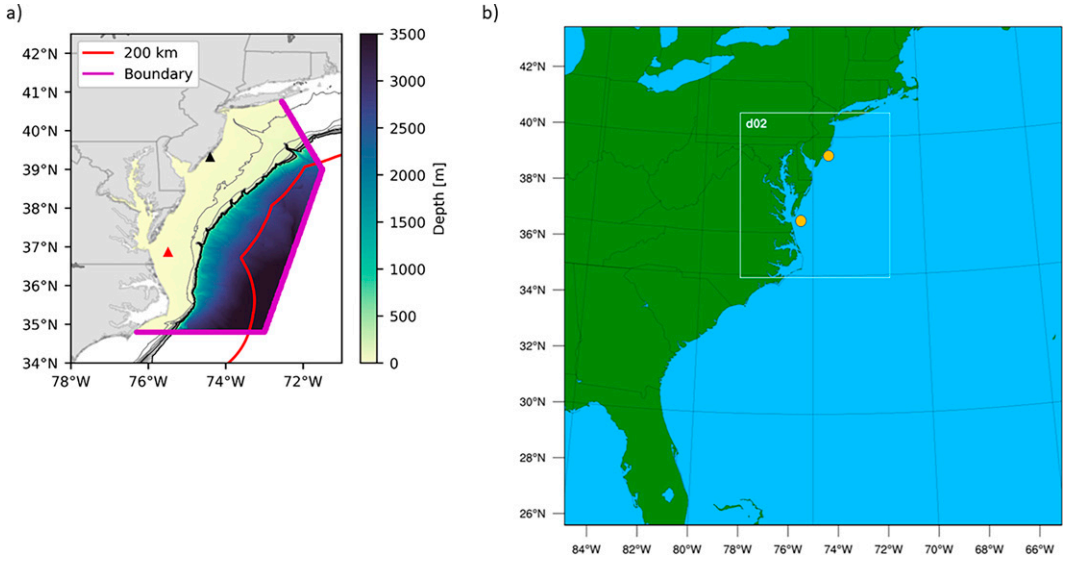

FIG. 3. (a) The mid-Atlantic Bight 2-km WW3 wave model domain. Colors represent the bathymetry in meters. Triangles indicate location of the two lidar buoys; (b) nested grid configuration used for WRF simulations. Yellow symbols indicate buoy locations.

TABLE 1. WRF namelist options selected for simulations in this study.

WRF namelist option	Value
Horizontal dimensions	134 × 134, 121 × 133
Horizontal grid spacing (km)	15, 5
Vertical dimension	72
Time step (s)	90, 30
Boundary layer parameterization	Mellor–Yamada–Nakinishi–Naiino (MYNN) with eddy diffusion/mass flux (EDMF)
Microphysics	WSM 6-class
Radiation	RRTMG
Convective parameterization	Kain–Fritsch
Land surface model	Noah
Data assimilation	Above-PBL analysis nudging (Grid 1 only)

making it a good choice to investigate oceanic/atmospheric coupling. In addition, spectral boundary conditions and surface currents are included as forcing in the stand-alone and two-way coupled simulations. Spectral boundary conditions are provided along the open boundary by a multimodel implementation of WW3 consisting of a global model, a 10-arc-min model covering the northwestern Atlantic, and a 4-arc-min model; all developed by NOAA and executed in-house. Surface currents come from the Hybrid Coordinate Ocean Model (HYCOM) Global Ocean Forecasting System 3.0 database which have a spatial resolution of 1/12° (≈9.3 km × 7.3 km in the meridional and zonal directions at 38°N, respectively) and output every 3 h (Halliwell 2004). The inclusion of surface currents in the wave model is important because of the Gulf Stream (Ardhuin et al. 2017) and inner-shelf currents which significantly affect the waves, particularly large wave events (García Medina et al. 2020).

In this study, the wind input and dissipation due to whitecapping are modeled using the Ardhuin et al. (2010) formulations. The linear wave growth source term is also activated in this implementation following Cavaleri and Malanotte-Rizzoli (1981). Nonlinear quadruplet interactions are modeled with the discrete interaction approximation (Hasselmann et al. 1985). Wave dissipation due to bottom friction and depth-induced wave breaking are simulated with the Hasselmann et al. (1973) and Battjes and Janssen (1978) formulations, respectively. Wave shoaling and refraction are also accounted for in the model simulation. The wave spectrum is discretized with 32 frequencies ranging from 0.035 to 0.672 Hz with a logarithmic increment of 1.1 and 36 directional bins.

b. *Stand-alone WRF*

While the CFSv2 product has high temporal resolution (1 h), its atmospheric component, derived from the atmospheric Global Forecast System (GFS) is relatively coarse in spatial resolution (0.5° or ~50 km in the mid-Atlantic Bight region). We thus developed a stand-alone WRF configuration to simulate the mid-Atlantic Bight region at higher spatial resolution, as described below.

We make use of two domains: a coarse domain with 15-km grid spacing covering most of the eastern United States, and a fine domain with 5-km grid spacing over the mid-Atlantic Bight, covering both buoy deployments (Fig. 3b). All analysis will be on the 5-km domain. There are 72 vertical levels, including 6 in the lowest 200 m, with the lowest half-level at approximately 10 m. Initial and lateral boundary conditions are obtained from the CFSv2 to be consistent with those from the stand-alone WW3 simulation and facilitate comparison to the one-way coupled WRF simulation described below. The simulations were performed with the same WRF code as provided in the COAWST system (except for modifications made to perform the one-way coupled simulations). More details on the model configuration are found in Table 1.

After about 3 days the WRF forecast fields would begin to drift away from the atmospheric state as discerned in the CFSv2 analysis. Thus, it was decided to use analysis nudging on Grid 1 above the model boundary layer top to help constrain large-scale model fields toward the analysis (Stauffer and Seaman 1994). Grid 2 was kept unconstrained (except for the lateral boundary conditions) so it could be used for physics sensitivity studies.

As in typical WRF applications, sea surface temperature (SST) is not modified by the WRF model itself over time, but is updated periodically (here, 3 h on the coarse grid, 1 h on the fine grid) from lower boundary files derived from sea surface temperatures in the CFSv2. Oceanic roughness heights are computed in the model surface layer scheme using the COARE3.0 algorithm (Fairall et al. 2003). This algorithm parameterizes the roughness length as a function of the friction velocity (e.g., the square root of the magnitude of the

TABLE 2. Biases (model − observation), root-mean-squared errors (RMSEs), centered root-mean-squared errors (CRMSEs), and correlation coefficients (corr) for model predictions of 90-m wind speed, as verified against the VA and NJ buoy lidar-derived values (when available). Model output are from the baseline stand-alone WRF simulation used in this study, and from the RAP analyses used in Sheridan et al. (2020), at 1-h temporal frequency.

	Baseline bias ($m\ s^{-1}$)	Baseline RMSE ($m\ s^{-1}$)	Baseline CRMSE ($m\ s^{-1}$)	Baseline corr	RAP bias ($m\ s^{-1}$)	RAP RMSE ($m\ s^{-1}$)	RAP CRMSE ($m\ s^{-1}$)	RAP corr
8 May 2015 VA (tropical cyclone)	−0.18	2.14	2.13	0.82	−2.50	3.57	2.54	0.74
18 Jan 2016 VA (nor'easter)	−0.04	2.63	2.63	0.76	−1.21	2.14	1.77	0.90
18 Jan 2016 NJ (nor'easter)	−0.01	1.84	1.84	0.91	−0.40	2.04	2.00	0.89
25 Mar 2016 VA (frontal passage)	0.36	2.71	2.68	0.79	−2.03	4.49	4.00	0.67
25 Mar 2016 NJ (frontal passage)	0.77	1.81	1.64	0.96	−1.67	2.75	2.19	0.93

TABLE 3. Biases (model − observation), RMSEs, centered root-mean-squared errors (CRMSEs), and correlation coefficients (corr) for model predictions of 90-m wind speed, as verified against the VA and NJ buoy lidar-derived values (when available). Model output are from the one-way coupled WRF configuration, and from two-way coupled WRF/WW3 configuration described in the text, at 1-h temporal frequency.

	One-way WRF bias ($m\ s^{-1}$)	One-way WRF RMSE ($m\ s^{-1}$)	One-way WRF CRMSE ($m\ s^{-1}$)	One-way WRF corr	Two-way WRF/WW3 bias ($m\ s^{-1}$)	Two-way WRF/WW3 RMSE ($m\ s^{-1}$)	Two-way WRF/WW3 CRMSE ($m\ s^{-1}$)	Two-way WRF/WW3 corr
8 May 2015 VA (tropical cyclone)	−0.45	2.07	2.03	0.83	−0.33	2.11	2.08	0.83
18 Jan 2016 VA (nor'easter)	−0.22	2.70	2.69	0.75	−0.05	2.74	2.74	0.74
18 Jan 2016 NJ (nor'easter)	−0.01	1.85	1.85	0.91	0.00	1.88	1.88	0.90
25 Mar 2016 VA (frontal passage)	−0.14	2.59	2.58	0.8	0.09	2.63	2.63	0.80
25 Mar 2016 NJ (frontal passage)	−0.32	2.11	2.08	0.95	−0.01	1.89	1.89	0.96

surface vertical momentum flux per mass), so is not directly dependent on wave state.

Boundary layer turbulent transport was predicted using the Mellor–Yamada–Nakanishi–Niino (MYNN) parameterization, with the eddy diffusion mass flux (MYNN-EDMF) option. Turbulent fluxes at the lower boundary were computed by the surface layer scheme option provided with MYNN. Most other physics options used were those recommended for use in the COAWST simulations of WRF.

c. *One-way coupled WRF*

In the one-way coupled WRF simulation, hourly output of significant wave height, peak wavelength, and period of peak wave were extracted from the stand-alone WW3 simulation and appended to the WRF Grid 2 lower boundary files. WRF was modified to read in and update these parameters along with SST. For Grid 1, and for regions of Grid 2 lying outside of the boundaries of the 2-km WW3 grid, wave parameters were instead extracted from the global WW3 model. Significant wave height and peak wavelength were then used in the model surface layer scheme to compute ocean roughness height according to a version of the of the Taylor and Yelland (2001) parameterization: $z_0 = 1200.0H_S(H_S/L)^{4.5} + 0.11\nu/u_*$, where H_S is significant wave height, L is mean wavelength of waves, ν is air kinematic viscosity, and u_* is friction velocity. Otherwise, the configuration of WRF remained the same.

d. *Two-way coupled WRF/WW3*

For the two-way coupled WRF/WW3 simulations, the COAWST framework is explicitly invoked. The WRF and 2-km WW3 configurations were kept as close as possible to those of the stand-alone versions, both in terms of grids and physics parameterizations. The coupling interval was chosen to be 1800 s. To maintain consistency with the stand-alone WW3, the HYCOM current fields used to drive the stand-alone WW3 simulation were used for the two-way version of WW3 as well. Only the 2-km WW3 was active.

e. *One-way coupled WW3*

Analogous to the one-way coupled WRF simulation, a stand-alone simulation of WW3 was performed, but this time using for wind input the results from the stand-alone WRF simulation. Other WW3 parameters are kept the same as in the stand-alone WW3 simulation. The purpose of this simulation will be to help isolate the impacts of different processes in the two-way coupled WRF.

4. Results

a. *Summary statistics*

Here we give summary statistics for the performance of the model configurations across selected cases from the buoy deployment. The cases shown are a tropical cyclone case from 0000 UTC 8 May 2015 to 1200 UTC 12 May 2015, a strong

TABLE 4. Biases (model − observation), centered root-mean-squared errors (CRMSEs), and correlation coefficients (corr) for model predictions of 4-m wind speed, as verified against the VA and NJ buoy values (when available). Model output are from the baseline stand-alone WRF configuration, from the one-way coupled WRF configuration, and from two-way coupled WRF/WW3 configuration described in the text, at 1-h temporal frequency. A similarity adjustment was used to extrapolate the model wind speed from the lowest model level (10 m) to the height of the buoy measurement (4 m).

	Baseline bias ($m\ s^{-1}$)	Baseline CRMSE ($m\ s^{-1}$)	Baseline correlation	One-way WRF bias ($m\ s^{-1}$)	One-way WRF CRMSE ($m\ s^{-1}$)	One-way WRF corr	Two-way WRF/WW3 bias ($m\ s^{-1}$)	Two-way WRF/WW3 CRMSE ($m\ s^{-1}$)	Two-way WRF/WW3 corr
8 May 2015 VA	−0.08	1.21	0.76	−0.19	1.10	0.77	−0.08	0.97	0.83
18 Jan 2016 VA	−0.62	2.03	0.79	−1.05	2.26	0.74	−0.88	2.13	0.78
18 Jan 2016 NJ	−1.28	1.41	0.92	−1.24	1.45	0.91	−1.19	1.47	0.91
25 Mar 2016 VA	0.21	1.70	0.39	−0.34	1.49	0.50	−0.23	1.50	0.55
25 Mar 2016 NJ	−0.49	1.43	0.92	−1.27	1.66	0.91	−0.99	1.52	0.92

nor'easter case from 1200 UTC 18 January 2016 to 0000 UTC 24 January 2016, and a cold frontal passage case from 0000 UTC 25 March 2016 to 0000 UTC 27 March 2016. More details on these cases will be discussed in later subsections, but they are ones for which the reanalysis products used in Sheridan et al. (2021) showed particularly large errors. Only the VA buoy was deployed for the tropical cyclone case, while for the other cases both buoys were deployed. However, during the 0000 UTC 25 March 2016–0000 UTC 27 March 2016 period, data were not available from the NJ buoy after 0100 UTC 26 March, so for that buoy, only the prior period is included in the statistics.

Table 2 shows wind speed biases (model − observations), root-mean-squared errors (RMSEs), centered root-mean-squared errors (CRMSEs), and correlation coefficients for the predictions of the baseline stand-alone WRF configuration as verified against the lidar-derived 90-m wind speeds from the buoys, at a temporal frequency of 1 h. Formulas for these metrics can be found in the appendix. The baseline wind speed prediction is found by interpolating between the third and fourth model vertical layers to 90 m MSL. Also shown in Table 1 for comparison are the corresponding hub-height statistics from the RAP analyses. For all of these cases RAP had RMSEs between 2 and 5 m s^{-1} in hourly wind speeds. (As discussed in Sheridan et al. (2020), these are taken from the RAP 0–30-hPa near-surface field, although other methods of determining RAP hub-height wind speed showed little difference.)

It can be seen in Table 2 that the 5-km stand-alone WRF configuration has substantially reduced 90-m biases (~1–2 m s^{-1}) from the RAP for all cases, which now never exceed 1 m s^{-1} in magnitude. WRF also has moderately improved correlation and RMSE statistics in most of the cases. The one exception is for the VA buoy during the 18 January 2016 case, for which the CRMSE and correlation coefficient are somewhat worse than those from the RAP, despite a near elimination of the wind speed bias.

We now show the corresponding statistics for the one-way WRF and two-way WRF/WW3 coupled simulations (Table 3). In general, the sensitivity of 90-m wind statistics to these modes of wave–atmosphere coupling is modest, and case-dependent. The use of waves in one-way WRF simulations does almost always make the baseline biases more negative (i.e., average wind speeds are reduced). For the 25 March 2016 case, including waves seems to improve the statistics, especially at VA, while for the 8 May 2015 case, the wave-including models have biases that are degraded from stand-alone WRF, though the CRMSEs were improved. For 18 January 2016, wave input seems to have a small and unclear impact on both one-way and two-way coupled simulations.

Comparing one-way versus two-way coupled statistics, we see that, while systematic differences between the two are small, the two-way simulation has biases that are both more positive than those of the one-way simulation, and reduced in magnitude (i.e., better). However, the one-way simulation tends to have slightly better CRMSEs than the two-way simulation.

To determine if these tendencies also hold closer to the surface, we repeat the analysis, but this time comparing the models to the buoy 4-m wind speed (Table 4). Since the lowest model level for horizontal wind speed is 10 m, we perform a similarity extrapolation of the model 10-m wind speed to the 4-m level first before computing the statistics. This method uses empirical functions of z/L, where z is height and L, the Obukhov length, is a measure of atmospheric stability, being positive in stable conditions and negative in unstable conditions. The similarity functions used are those applied in the COARE3.0 algorithm, based on those of Businger et al. (1971), Beljaars and Holtslag (1991), and Grachev et al. (2000).

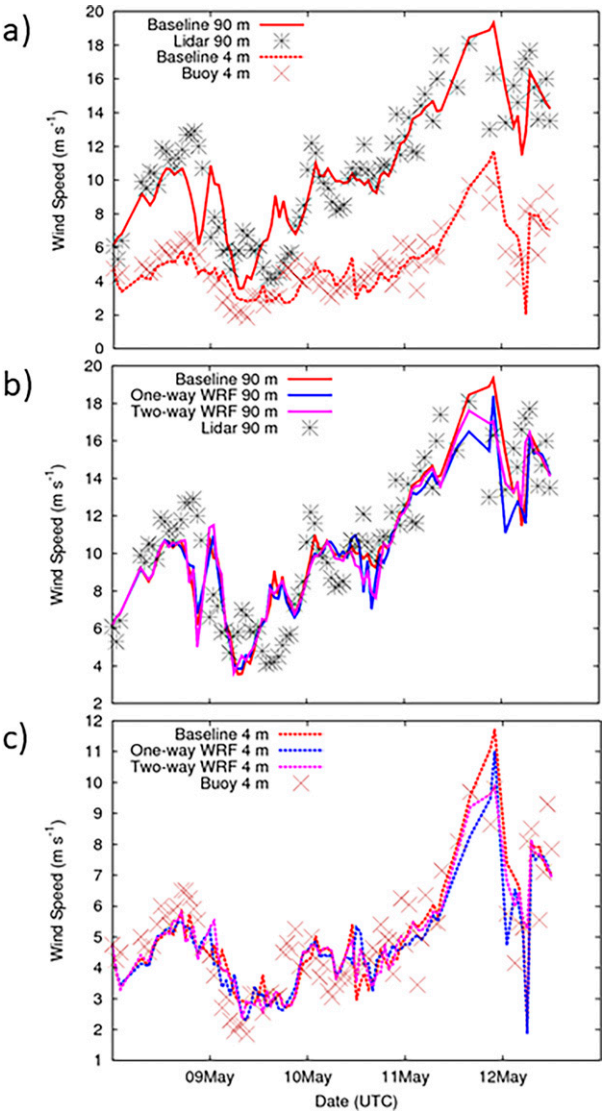

FIG. 4. Observed and model wind speeds for the 0000 UTC 8 May 2015–1200 UTC 12 May 2015 case at the VA buoy: (a) observed and baseline model 90- and 4-m wind speeds; (b) observed, baseline, one-way wave-coupled WRF, and two-way wave-coupled WRF 90-m wind speeds; and (c) observed, baseline, one-way wave-coupled WRF, and two-way wave-coupled WRF 4-m wind speeds. Model 90-m wind speed is interpolated; model 4-m wind speed is extrapolated from 10 m.

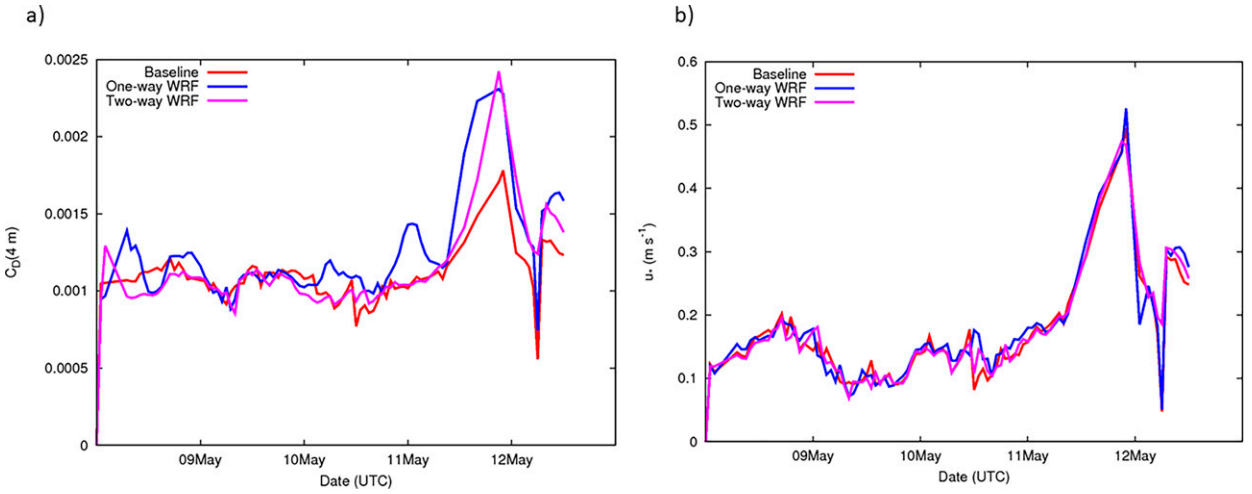

FIG. 5. Comparison of (a) 4-m drag coefficient and (b) friction velocity for baseline, one-way wave-coupled WRF, and two-way wave-coupled WRF simulations for the 0000 UTC 8 May 2015–1200 UTC 12 May 2015 case at the VA buoy.

For the 4-m wind speed we again see that one-way coupled WRF is almost always more negatively biased than the baseline, while the two-way simulation has biases less negative and reduced in magnitude than the one-way. We also see that, for the VA cases at least, the 4-m wind speed correlation coefficients are noticeably better in the two-way than in the one-way simulations. Interestingly, for the 25 March 2016 case all the correlation coefficients are low (~0.55 for the 25 March 2016 case with two-way wave coupling, and even worse for the baseline and one-way coupling). At the NJ buoy, the correlation coefficients are excellent (over 0.9), but large negative biases (often around -1 m s^{-1}) exist for all models at this location.

To gain more insight into these tendencies, we examine the individual cases in more detail.

b. Case 1: 8 May 2015, Tropical Storm Ana

During this case period, Tropical Storm Ana made landfall near Myrtle Beach, South Carolina, the morning of 10 May 2015, becoming the earliest landfalling Atlantic Basin tropical cyclone for the United States on record. It entered Chesapeake Bay as a tropical depression around 1800 UTC 11 May, and then tracked up the Maryland Eastern Shore, passing just northwest of the VA buoy location.

Time series of 90- and 4-m wind speeds for the baseline simulation and the buoy are shown in Fig. 4a. The observed 90-m wind speed increases toward a peak around 18 m s^{-1} at 1600 UTC 11 May. Unfortunately, 90-m data are absent from then until 2100 UTC, so the exact time of peak 90-m wind cannot be determined. The 4-m wind at the buoy peaks near 13 m s^{-1} between 1800 and 1900 UTC while the 4-m wind direction rotates from southeast to southwest, associated with the system moving north of the buoy. Thus the true 90-m peak wind probably occurs around this time and is at least 18 m s^{-1}. The baseline configuration does well at tracking the observations at longer time scales, but hour-to-hour fluctuations in the observed wind speed are not well captured.

In Figs. 4b and 4c we compare the wind speeds between the different model configurations. Very little difference appears among them until approximately 6 h before the time of peak wind speed in the southeast flow (1300 UTC 11 May). From this point until peak wind speed the one-way WRF simulation has 90-m wind speed 1–3 m s^{-1} less than that of the baseline (Fig. 4b). The two-way WRF is generally intermediate between the baseline and the one-way. The peak 90-m wind in the two-way seems to be the closest match to the observations in both value and timing, though the 90-m data gap makes this difficult to determine precisely. The same trends appear in the 4-m model winds (Fig. 4c), though with somewhat smaller differences.

In Fig. 5a we show the effective model drag coefficients at the VA buoy location at 4 m (C_D), which in neutral conditions is a function of the roughness length [$C_{DN} = k^2/\ln(4\text{ m}/z_0)^2$], but is increased/decreased in stable/unstable conditions. We also show the model friction velocities in Fig. 5b, given by $u_* = \sqrt{C_D}U_{4m}$ where U_{4m} is the 4-m wind speed. We see that all simulations have virtually the same friction velocity, with a single sharp peak. The baseline and two-way simulations have peaks in drag coefficients corresponding to the peak in friction velocity, with greater drag coefficients in the two-way corresponding to reduced 4-m wind speeds. For the one-way simulation the drag coefficient has a similar peak value to that of the two-way simulation, but has substantially greater drag during the preceding period when its wind speeds are suppressed relative to the two-way.

To indicate the spatial extent of the one-way versus two-way wave coupling sensitivity, we show the model 90-m wind fields and roughness heights for the two simulations at 1600 UTC 11 May (Fig. 6) during the approach to peak wind speed in both models and observations. It can be seen that the roughness heights are enhanced in the one-way versus the two way simulation at the VA buoy location and in a zone extending to the southeast. It can also be seen that the period of suppressed winds in the one-way simulation

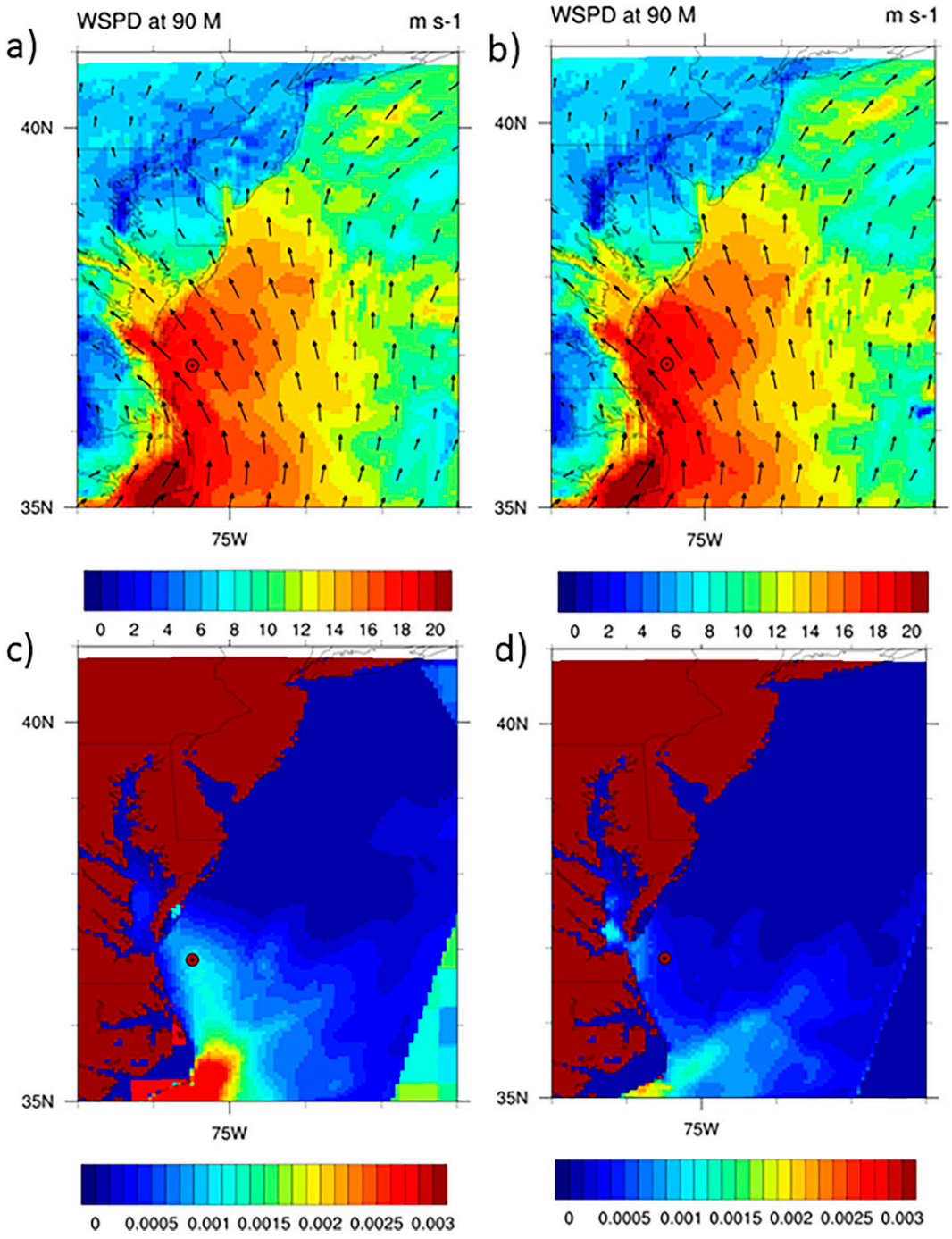

FIG. 6. Comparison between (a),(c) one-way WRF simulation and (b),(d) two-way WRF/WW3 simulation at 1600 UTC 11 May 2015. (top) The 90-m wind speed vectors and magnitude (shaded; m s^{-1}). (bottom) Ocean roughness length (m). Circle indicates location of VA buoy; circle shading in the top row indicates observed 90-m wind speed.

corresponds to the time when the prevailing wind at the VA buoy is directed from the region where the oceanic roughness is enhanced.

These results are consistent with the sea state evaluation. To give a holistic view of the impact of the higher resolution wind fields on the waves, model wave output and data are compared across several buoy stations in the vicinity of the event. We evaluate the original stand-alone WW3 (i.e., driven by CFSR, and providing the wave input to one-way WRF), WW3 from the two-way WRF/WW3 simulation, and the one-way coupled WW3 simulation driven by the baseline WRF winds. We include this third simulation because

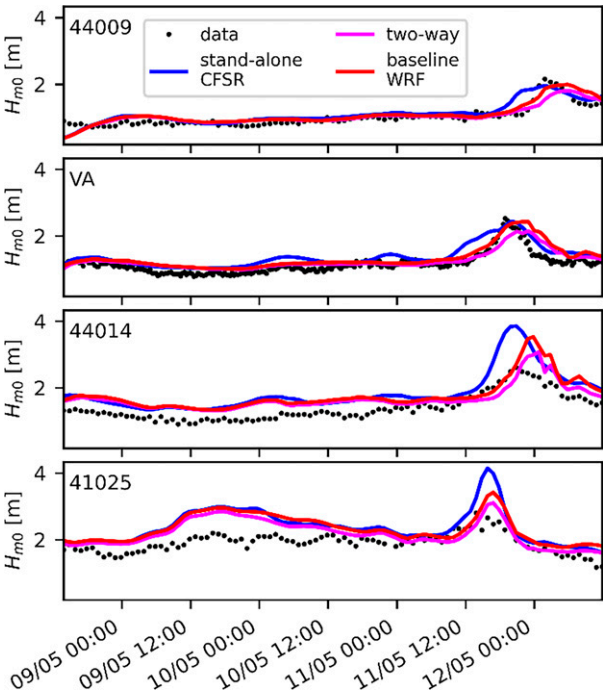

FIG. 7. Comparison of significant wave height at buoys near the south of the domain during Case 1 at selected buoy stations.

differences between the stand-alone WW3 and two-way WW3 wave fields might be due to either a feedback-type interaction between winds and waves (e.g., increased wave heights might increase momentum drag on the winds, reducing wind speeds, which in turn decreases wave growth rates), or due to other differences between the two wind driver fields involved (CFSR at roughly 40-km effective grid spacing versus WRF at 5 km).

Time series of significant wave height are shown in Fig. 7. WW3 shows similar performance in the three model configurations before Tropical Storm Ana approaches the coast, but then stand-alone WW3 wave height predictions tend to peak too early and too high relative to both the other models and the observations. Overprediction of wave height in the stand-alone WW3 case is associated with a greater spatial area of elevated wind speeds in CFSR versus that in the WRF baseline and two-way interactive simulations. The relative closeness of two-way and baseline-driven WW3 versus stand-alone CFSR-driven WW3 suggests that the difference in wind driver is the major contributor to the stand-alone/two-way WW3 difference. However, a consistent suppression of maximum significant wave heights in the two-way relative to baseline-driven could reflect a negative coupling feedback.

A quantitative assessment over the same period shown in Fig. 7 indicates a progressive improvement in significant wave height statistics from the stand-alone WW3 to the one-way coupled simulation to the two-way simulation in virtually all cases (Table 5). These tendencies are not quite as clear for mean wave period, but usually statistics for the two

TABLE 5. Number of observations, root-mean-squared errors, biases (model − observation), and absolute percent error for significant wave height and mean wave period during the hindcast period for the stand-alone WW3 (CFSR winds), one-way coupled WW3 (WRF baseline winds) and two-way coupled WW3 models during Case 1 (8 May 2015).

		Significant wave height (m)								Mean wave period (s)							
		RMSE			Bias			APE		RMSE			Bias			APE	
Station	N	Stand-alone	One-way	Two-way	Stand-alone	One-way	Two-way	Stand-alone	One-way	Two-way	Stand-alone	One-way	Two-way	Stand-alone	One-way	Two-way	Stand-alone	One-way	Two-way
44065	83	0.20	0.18	0.17	0.09	0.04	0.03	12.3	5.8	6.4	0.78	1.10	0.93	−0.55	−0.80	−0.67	9.7	14.3	11.7
44025	83	0.34	0.20	0.22	0.29	0.12	0.12	34.3	15.8	17.4	0.93	1.0	0.84	−0.69	−0.67	−0.51	11.9	10.7	8.3
NJ	—	—	—	—	—	—	—	—	—	—	—	—	—	—	—	—	—	—	—
44009	83	0.18	0.16	0.15	0.11	0.07	0.03	11.9	7.1	5.3	0.76	0.89	0.61	−0.64	−0.25	−0.53	11.2	4.5	9.4
44096	165	0.12	0.12	0.09	0.04	0.02	−0.02	5.3	2.4	1.2	0.81	0.76	0.80	−0.71	−0.61	−0.66	13.9	11.8	12.7
44099	162	0.14	0.14	0.09	0.07	0.05	0	7.4	4.8	0.3	0.80	0.67	0.72	−0.72	−0.56	−0.63	13.5	10.5	12.0
44093	165	0.21	0.18	0.16	0.16	0.10	0.03	13.7	8.7	4.1	0.91	0.70	0.73	−0.83	−0.61	−0.67	14.7	11.0	12.0
VA	285	0.25	0.23	0.20	0.21	0.16	0.10	19.5	14.8	10.3	0.41	0.38	0.35	−0.17	0.05	−0.03	3.0	1.5	0.3
44014	83	0.53	0.44	0.35	0.46	0.38	0.26	33.3	29.4	22.1	0.47	0.33	0.34	−0.34	−0.24	−0.25	6.0	4.2	4.5
44100	163	0.19	0.21	0.18	0.14	0.12	0.04	11.9	10.6	4.0	0.96	0.76	0.78	−0.86	−0.69	−0.72	15.8	12.8	13.3
44095	162	0.34	0.29	0.21	0.23	0.21	0.07	14.3	14.3	5.3	0.53	0.43	0.43	−0.44	−0.35	−0.36	8.2	6.4	6.7
41025	81	0.60	0.52	0.41	0.50	0.43	0.28	25.6	23.2	15.2	0.27	0.29	0.27	−0.06	0.01	0.11	1.2	0.4	2.0

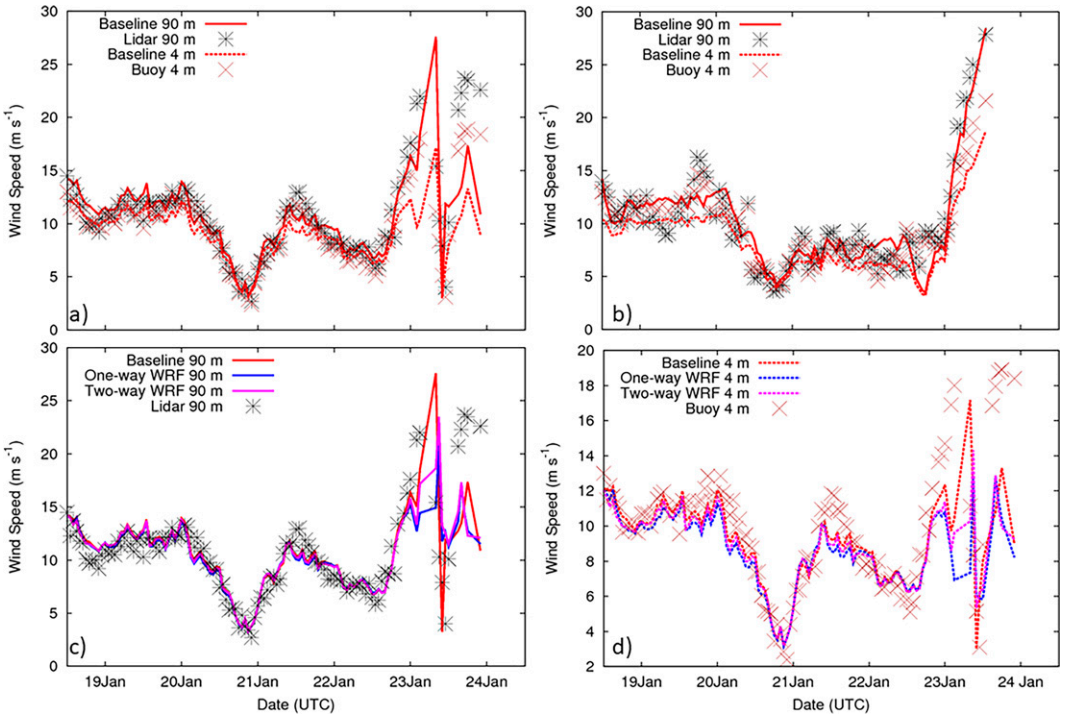

FIG. 8. Observed and model wind speeds for the 1200 UTC 18 Jan 2016–0000 UTC 24 Jan 2016 case: (a) observed and baseline model 90- and 4-m wind speeds at the VA buoy; (b) observed and baseline model 90- and 4-m wind speeds at the NJ buoy; (c) observed, baseline, one-way wave-coupled WRF, and two-way wave-coupled WRF 90-m wind speeds at the VA buoy; and (d) observed, baseline, one-way wave-coupled WRF, and two-way wave-coupled WRF 4-m wind speeds at the VA buoy. Model 90-m wind speed is interpolated; model 4-m wind speed is extrapolated from 10 m.

WRF-driven simulations are better than those of standalone WW3.

c. *Case 2: 18 January 2016, East Coast nor'easter*

From 22 to 24 January 2016, a strong winter storm system impacted the U.S. East Coast, producing up to three feet of snow in some areas. This "nor'easter" began as a low pressure center in the Gulf Coast before it moved up the Carolina coast. The low pressure center crossed into the Atlantic near the North Carolina–Virginia border at 1200 UTC 23 January, just south of the location of the VA buoy. To track the full development of the storm, the WRF simulations were begun on 1200 UTC 18 January 2016, extending to 0000 UTC 24 January 2016.

As might be expected, both buoys recorded large wind speeds and wave heights with the event (Fig. 8)—in fact, the greatest significant wave heights of the whole buoy deployment (García Medina et al. 2020). Peak wind speed for the VA buoy occurred just prior to 0600 UTC 23 January at 4 m; the peak recorded speed at 90 m occurred at 0300 UTC, but no data were recorded at this level between 0400 and 0700 UTC. Peak wind speed for the NJ buoy was occurring right when data cut out at 0000 UTC 24 January. At the VA buoy location there is a double maximum in wind speed as the low pressure center passes by, of roughly equal magnitude at 90 m (20–25 m s^{-1}). The baseline configuration overestimates the magnitude of the first peak by 2 m s^{-1} (but again, it is possible the actual peak 90-m wind speed was not observed), while it underestimates the second (6.4 m s^{-1}). Buoy-level winds are slightly underestimated at the first peak, by about 1 m s^{-1}, but delayed to 0800 UTC; at the second peak 4-m winds, like 90-m winds, are significantly underestimated (by 5.6 m s^{-1}). At the NJ buoy location, the baseline prediction of the peak hub-height wind correlates well with observations, but the buoy-level winds are again underestimated (by about 2 m s^{-1}). It should also be noted that the underestimation of buoy-level winds is present throughout the simulation time period at the NJ buoy, and to some degree at the VA buoy location, although less pronounced.

This seems to be a case where the large model wind speed errors are due to errors in the general forecast meteorology on the 5-km domain, despite the use of analysis nudging on the parent domain. From about 0000 to 0500 UTC 23 January, while the observed wind speeds were rapidly increasing, the observed wind direction was from the east-northeast versus east-southeast in the model, with a 20°–30° error; the surface air temperature also increased substantially more in the model than in the observations, by over 3°C at 0500 UTC. During the time of the second wind speed maximum, the wind direction errors are even worse (observed winds from

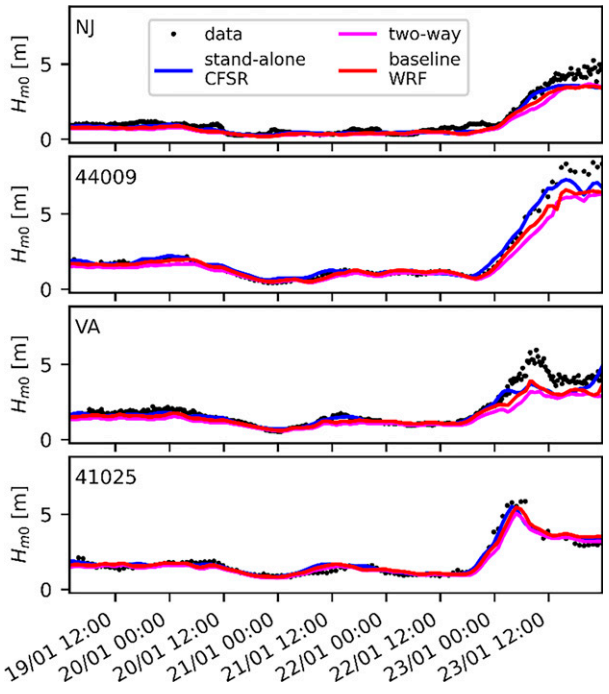

FIG. 9. Comparison of significant wave height at buoys near the south of the domain during Case 2 at selected buoy stations.

west-northwest, model winds from west-southwest, error about 50°).

It is thus likely that development and track forecast errors with this very heterogeneous system lead to the large model wind errors relative to the VA buoy. Recall that this is the one case where the RAP analysis product outperformed stand-alone 5-km WRF in terms of 90-m wind statistics.

The effects of near-surface wind speed underestimation at the lidar buoys are reflected in a generalized underestimation of significant wave height (Fig. 9). The stand-alone WW3 simulation shows better comparison with the wave data at the time of the nor'easter, though all models underpredict the largest wave heights across multiple buoys. Before 0000 UTC 23 January all models show very similar performance. The error in the wave period is also larger in the two-way nested simulation for all but one of the analyzed buoys (see Table 6).

d. *Case 3: 25 March 2016, cold frontal passage*

During the day of 25 March 2016 a strong low pressure system moved northeast along the St. Lawrence River Valley in Canada, while a trailing cold front extended SSW all the way to the Gulf of Mexico. In the mid-Atlantic Bight region, this period was characterized by the cold frontal passage, involving wind directions changing from southwest to northeast over a broad region along the Atlantic seaboard.

For this case, the wind speed predictions of the baseline configuration at the VA buoy are generally good, at least at time scales of several hours or more (Fig. 10). However, the model frontal passage, as marked by the wind shift, is slightly early (0000 UTC 26 March, versus after 0200 UTC 26 March in the

TABLE 6. As in Table 5, but for Case 2 (18 Jan 2016).

		Significant wave height (m)								Mean wave period (s)							
		RMSE			Bias		APE			RMSE			Bias		APE		
Station	N	Stand-alone	One-way	Two-way	Stand-alone	One-way	Two-way	Stand-alone	One-way	Two-way	Stand-alone	One-way	Two-way	Stand-alone	One-way	Two-way	Stand-alone	One-way	Two-way
44065	1107	0.24	0.26	0.36	−0.16	−0.01	−0.17	19.0	4.6	7.9	0.73	0.62	0.71	−0.70	−0.54	−0.66	18.7	13.7	16.9
44025	107	0.22	0.27	0.39	−0.05	−0.03	−0.20	5.3	4.9	5.8	0.64	0.59	0.71	−0.60	−0.54	−0.64	13.9	11.8	14.5
NJ	321	0.32	0.41	0.49	−0.16	−0.28	−0.35	10.4	21.0	27.5	0.73	0.55	0.66	0.03	−0.08	−0.14	0.2	4.5	6.8
44009	106	0.39	0.53	0.77	0.01	−0.22	−0.44	9.3	3.1	13.9	0.52	0.65	0.82	−0.45	−0.59	−0.73	9.0	12.0	14.9
44096	179	0.67	0.70	0.88	−0.34	−0.36	−0.52	12.9	12.3	22.0	0.84	0.82	0.95	−0.57	−0.57	−0.71	10.7	11.5	14.1
44099	179	0.60	0.59	0.79	−0.29	−0.30	−0.49	10.0	9.4	19.8	0.58	0.61	0.78	−0.43	−0.47	−0.62	8.0	9.4	12.4
44093	—	—	—	—	—	—	—	—	—	—	—	—	—	—	—	—	—	—	—
VA	321	0.43	0.54	0.76	−0.14	−0.31	−0.51	4.4	10.3	20.5	0.52	0.32	0.49	−0.10	−0.12	−0.27	1.2	2.2	5.4
44014	107	0.42	0.45	0.72	−0.10	−0.23	−0.50	1.2	5.3	16.8	0.59	0.65	0.86	−0.49	−0.57	−0.78	8.5	10.3	14.1
44100	180	0.52	0.44	0.61	−0.26	−0.25	−0.42	8.0	8.9	17.8	0.88	0.86	1.02	−0.66	−0.73	−0.88	11.1	13.2	15.7
44095	178	0.50	0.42	0.59	−0.24	−0.28	−0.46	7.1	10.6	19.0	0.99	0.99	1.13	−0.82	−0.86	−1.01	13.4	14.6	17.0
41025	1107	0.28	0.31	0.39	0.01	−0.01	−0.16	3.5	1.9	5.6	0.74	0.74	0.82	−0.64	−0.64	−0.70	11.9	12.0	13.2

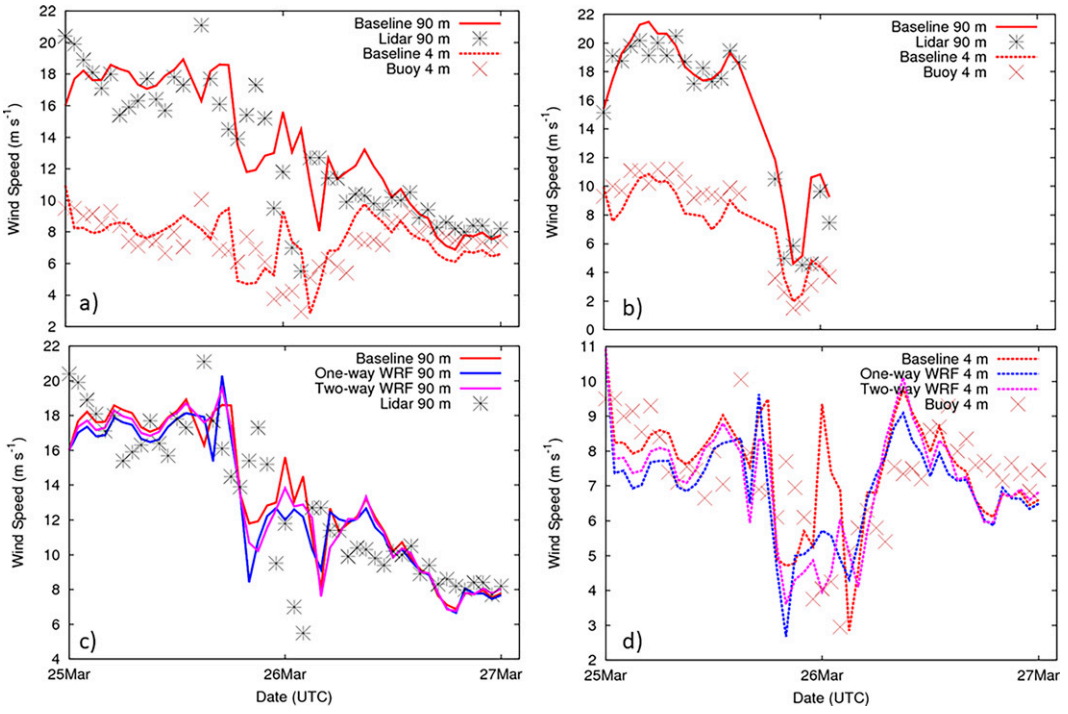

FIG. 10. Observed and model wind speeds for the 0000 UTC 25 Mar 2016–0000 UTC 27 Mar 2016 case: (a) observed and baseline model 90- and 4-m wind speeds at the VA buoy; (b) observed and baseline model 90- and 4-m wind speeds at the NJ buoy; (c) observed, baseline, one-way wave-coupled WRF, and two-way wave-coupled WRF 90-m wind speeds at the VA buoy; and (d) observed, baseline, one-way wave-coupled WRF, and two-way wave-coupled WRF 4-m wind speeds at the VA buoy. Model 90-m wind speed is interpolated; model 4-m wind speed is extrapolated from 10 m.

observations); there is also a wind speed peak immediately after frontal passage in the baseline simulation not reflected in the observations. Substantial variability is shown among all the model configurations around the time of frontal passage, while by around 1200 UTC 26 March the models all converge and tend to be closer to the observations. It can be seen that in the prefrontal regime considerable vertical wind shear exists, ~10 m s^{-1}, whereas after frontal passage 90-m wind speeds, and thus vertical shear, is far reduced; the vertical shear reduction is consistent with the change from stable to unstable atmospheric conditions. Data from the NJ buoy is only available from the first part of this simulation period; when they are present, the model predictions are good, although buoy-level wind speeds are again underestimated at this location.

Prior to about 0600 UTC 25 March, the two-way wind speed is between the one-way and baseline wind speeds both at 4 and 90 m AGL, with smaller differences at 90 m. From 0600 UTC up to and including the time of frontal passage, there are intermittent periods where model wind speed is sensitive to the method of wave coupling, but it is hard to find systematic trends. After frontal passage, the simulation with one-way coupling seems to have reduced wind speeds at 4 m compared to the other models until 1200 UTC 26 March, but otherwise there is not much postfrontal wind variability among the models.

We now examine domain-wide behavior for a sample prefrontal time (1500 UTC 25 March) and postfrontal time (1200 UTC 26 March). At 1500 UTC 25 March (Fig. 11), 90-m southwest winds exceeding 20 m s^{-1} exist along the coastline from Chesapeake Bay all the way to Long Island. This feature occurs in stable conditions—SSTs colder than air temperatures—and in fact the strongest winds to the north occur where the SSTs are the lowest over shelf waters. In the one-way WRF simulation (middle panels), we see that waves significantly increase roughness heights in both the southern and northern parts of the WW3 domain. In the northern part, the increased roughness is associated with 90-m wind speeds reduced by over 2 m s^{-1}, about 10%. Interestingly, wind speeds are not much reduced, if at all, in the southern part, which could be due to both lower overall wind speeds, and a limited wind fetch over the region. In the two-way simulation (right panels), results are qualitatively similar to the one-way simulation, except for somewhat less wave impact on wind speed than in the one-way simulation (reductions on the order of 1 m s^{-1} relative to the baseline).

A statistical analysis of the model wind speed sensitivities at 1500 UTC 25 March to wave coupling method (Figs. 12a,b) confirms that this case is predominantly stable. There is considerable vertical wind shear between 10 and 90 m for the stable cases and somewhat less for the neutral cases, as would be expected from similarity theory. By comparing winds in the one-way coupled simulation with the baseline (Fig. 12a), it is clear that the wave effects reduce wind speeds, although by no means universally. The median reduction of wind speed at 90 m for stable cases with wind > 10 m s^{-1} is about 10%. The

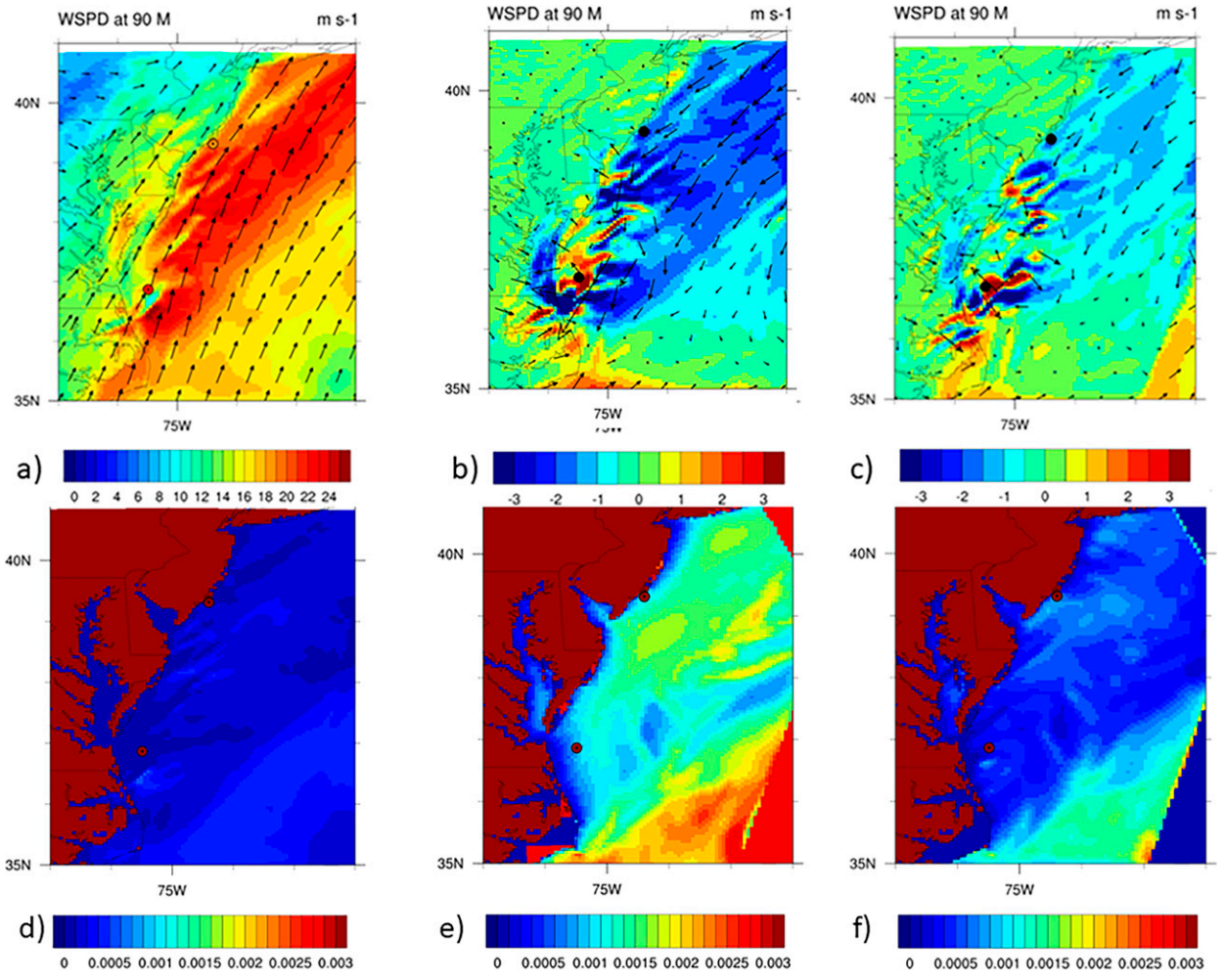

FIG. 11. (a) 90-m wind speed (m s^{-1}) and vectors at 1500 UTC 25 Mar 2016 in the 5-km domain for baseline simulation, (b) differences in 90-m wind speeds and vectors in the one-way WW3/WRF simulation from the baseline simulation, and (c) differences in 90-m wind speeds and vectors in the two-way WW3/WRF simulation from the baseline simulation. Roughness heights (m) over water for (d) the baseline simulation, (e) one-way WW3/WRF simulation, and (f) two-way WW3/WRF simulation. Circle indicates position of VA buoy. Circle shading in (a) indicates observed 90-m wind speed at each buoy.

comparison between one-way and two-way coupling (Fig. 12b) shows that systematic differences between the two are small, though large outliers of either sign exist (up to 8 m s^{-1} in magnitude). The overall median reduction of wind speed from baseline to one-way is about 1 m s^{-1} at both 90 and 10 m; from one-way to two-way causes a median wind speed increase approximately half that amount.

We now consider corresponding statistics for 1200 UTC 26 March. After the frontal passage, atmospheric conditions have become predominantly unstable (Figs. 12c,d). Only outliers in one-way WRF reduce 90-m wind speeds by as much as 10%, and the percent reduction drops off quickly once wind speeds fall below about 10 m s^{-1}; the median wind speed reduction is only 0.26 m s^{-1} at 90 m AGL. Two-way relative to one-way causes very little change in wind speeds, except for a slight increase for weak-wind neutral cases.

There is, however, the evidence that at the VA buoy location the 4-m wind speeds in one-way coupled WRF are somewhat less than those in two-way coupled WRF, or baseline WRF, for much of the initial postfrontal period (see Fig. 10d, about 0900–1400 UTC 26 March). If the time series of the 4-m drag coefficients are plotted (Fig. 13), this period corresponds to substantially reduced drag in the two-way versus one-way simulation. (Similarly elevated one-way drag coefficients appear in the prefrontal period as well. The initially elevated two-way drag coefficients before 1200 UTC 25 March occur prior to the wave field becoming fully spun up in that simulation.)

We now directly examine the time series of wave parameters in the WW3 models (stand-alone WW3, two-way WW3, and one-way baseline-driven WW3) at the location of buoys in comparison to observations for the 25 March 2016 case (Fig. 14a). We do not show the time series at the VA buoy location because of an issue with the updating frequency of

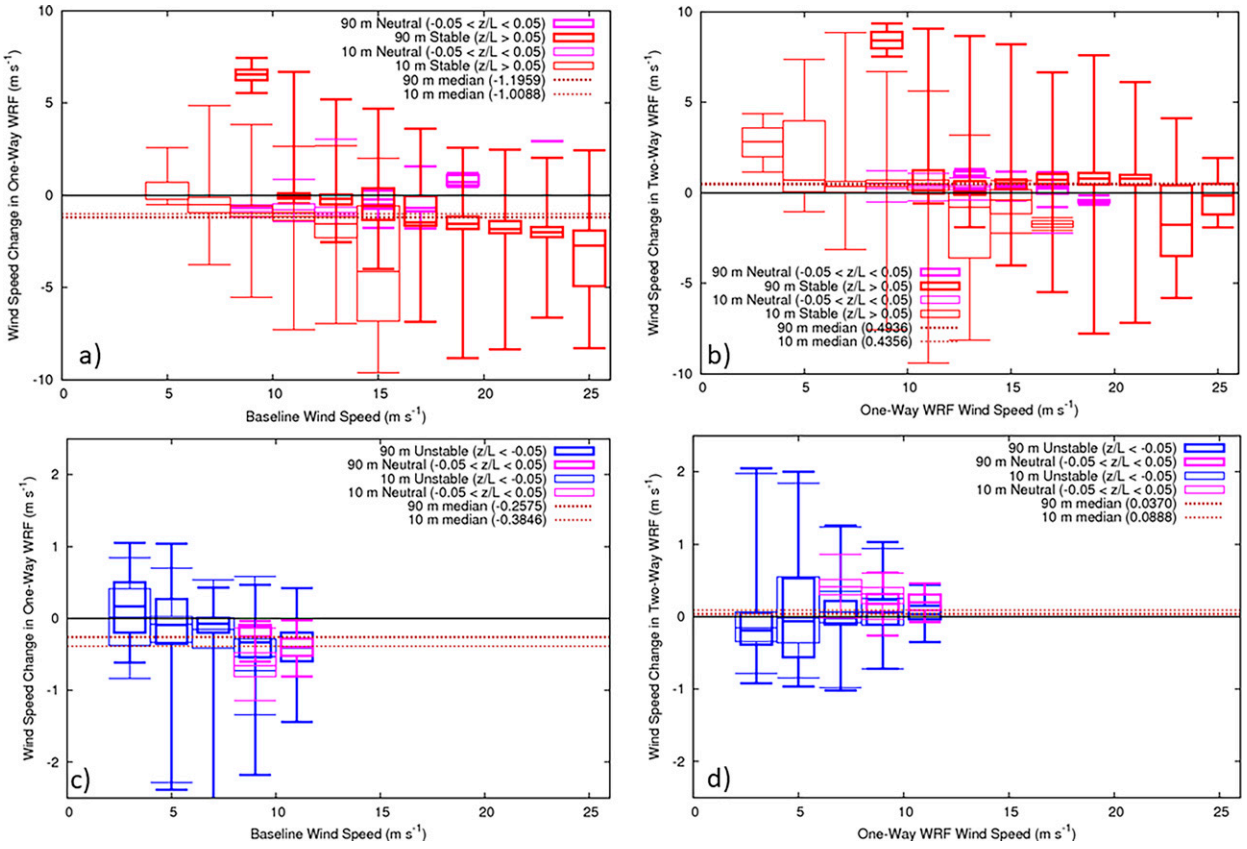

FIG. 12. Box-and-whisker plots for difference between: (left) one-way wave-coupled WRF simulated wind speeds and baseline simulated wind speeds and (right) two-way wave-coupled WRF simulated wind speeds and one-way wave-coupled WRF simulated wind speeds for 25 Mar 2016 case. (a),(b) Valid for 1500 UTC 25 Mar 2016 and (c),(d) valid 1200 UTC 26 Mar 2016. Boxes indicate interquartile range, binned every 2 m s^{-1}. Thick lines are for 90-m wind speed, while thin lines are for 10-m wind speed. Color indicates stability (z/L). Statistics are for each oceanic grid cell located in WW3 domain in two-way wave-coupled WRF simulation and away from the 5-km domain lateral boundaries. Horizontal dashed lines indicate overall median value of difference for each level. Note difference in vertical scale between (a),(b) and (c),(d).

wave data, but buoy 44093 in the figure is only a few km to the north (see Fig. 1a). The models are not perfect, but when stand-alone and two-way differ, the two-way configuration is almost always closer to the observations. In particular, at buoy 44093 overestimation of significant wave height in the stand-alone WW3 simulation can be seen from 0400 to 1200 UTC, corresponding to the time of elevated drag coefficients. Similarly to previous cases, forcing WW3 with the baseline WRF simulation produces results intermediate between the stand-alone and the two-way nested simulation but closer to the latter, although exceptions to this trend exist. Table 7 confirms that two-way RMSEs are usually as good as or better than stand-alone RMSEs for significant wave height (although not for mean wave period).

More details about the differences between modeled and observed wave characteristics at buoy 44093 can be seen in Fig. 14b, showing variance as a function of direction and frequency. At 0600 UTC, stand-alone WW3 shows waves propagating from the north, while the data and the WRF-forced simulations are still dominated by low-frequency swell from the southeast. Northeasterly waves are beginning to appear in the two-way WW3/WRF simulation by 0900 UTC, but much weaker than in stand-alone WW3, while the observations are beginning to show easterly waves. By 1200 UTC, buoy measurements and the models all agree on the presence of northeasterly waves of 0.2–0.3 Hz, though stand-alone WW3 overestimates the magnitude. Thus it seems the improved 4-m wind forecasts near the VA buoy location in the two-way simulation are directly related to the improved wave height forecasts in the wind sea (high frequency) band of the spectrum. The presence of locally generated winds at the correct timing suggests quantifiable improvements in the wind predictions by implementing a high resolution WRF model.

5. Discussion and conclusions

We have shown that using a 5-km WRF configuration can produce large improvements in predictions of both hub-height and buoy-height offshore wind speeds for a variety of cases during the East Coast lidar buoy deployment for which

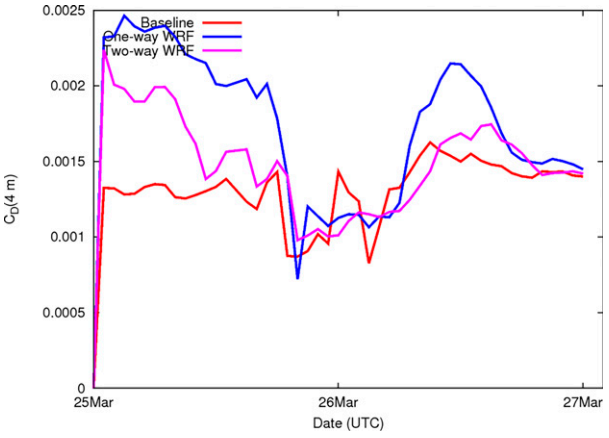

FIG. 13. Comparison of 4-m drag coefficient for baseline, one-way wave-coupled WRF, and two-way wave-coupled WRF simulations for the 0000 UTC 25 Mar 2016–0000 UTC 27 Mar 2016 case at the VA buoy.

conventional reanalysis products, at coarser horizontal and vertical resolution, had difficulties. The improvement occurred both in terms of wind speed biases and model/observation correlations. This suggests that many of the largest errors in modeling offshore hub-height wind might be due to insufficient resolution to properly capture the strength and timing of specific meteorological features.

The use of explicit wave-based roughness in one-way coupled WRF consistently reduced winds speeds across all cases, not only at buoy-height (4 m), but hub-height as well (90 m), especially in more stable conditions, where the reduction could be as much as 10%. This improved 90-m wind statistics relative to the VA lidar buoy for the 25 March 2016 frontal passage case, but increased a negative bias for the 8 May 2015 tropical cyclone case.

When a two-way coupled WRF/WW3 framework was used for these cases, the negative wind speed biases of the one-way WRF were mitigated, both at 4 and 90 m. The two-way coupled simulations also tended to produce wave fields closer to buoy observations than the one-way simulation, and better 4-m wind correlation statistics. Large differences between one-way WRF and two-way WRF wind fields tended to be associated with large differences in the modeled wave heights and mismatches between wind and wave fields, primarily due to the different wind fields used for stand-alone versus WRF-driven WW3, and secondarily due to the impact of two-way interaction.

For the 18 January 2016 nor'easter case, model meteorological errors precluded clear forecast improvement from the use of wave coupling. The better performance of RAP for this case might be due to its data assimilation, or its greater geographical coverage for this large system. In addition, for these particular systems oceanic heat and moisture fluxes have a great impact on storm strength and evolution. These fluxes are functions of atmospheric stability and air/sea temperature differences, and a fully three-way coupled ocean–wave–atmospheric modeling system would be expected to predict them better.

Frequently there were negative biases in the model buoy-level wind speed for the NJ buoy, or for offshore wind directions, even when the 90-m wind speed was roughly correct. Since the NJ buoy is closer to shore (5 km) than the VA buoy (30 km), this may reflect the fact that the baseline WRF configuration is still insufficient to properly resolve flows in the near-coastal environment in some cases.

These results demonstrate that the combination of sufficiently high resolution and constrained model simulations,

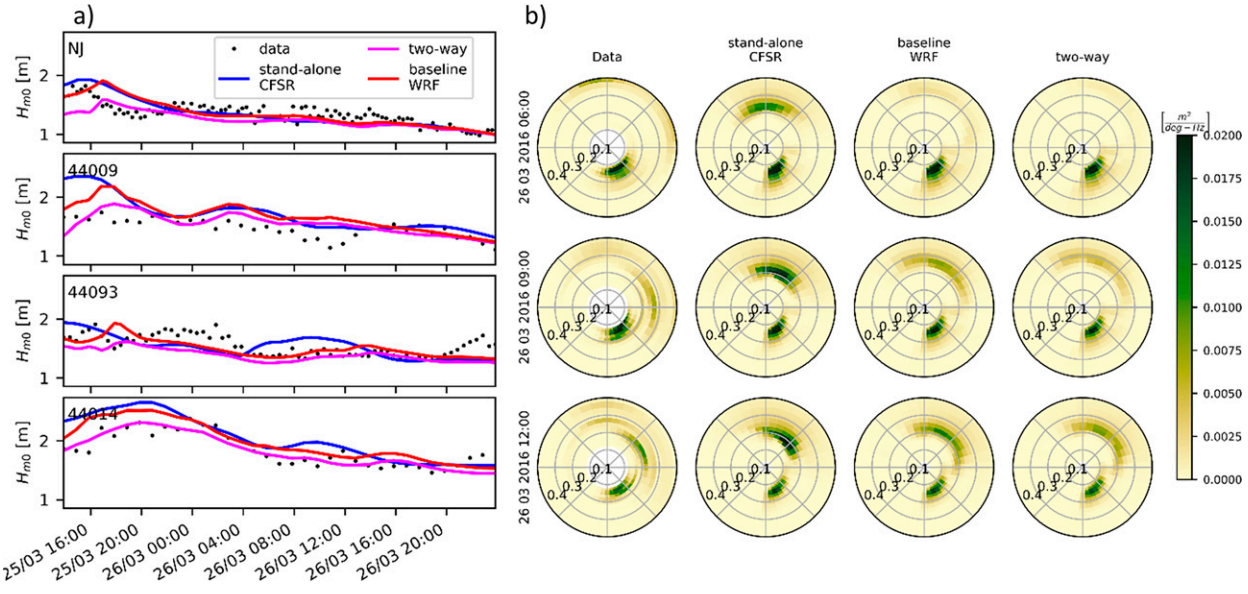

FIG. 14. (a) Comparison of significant wave height at buoys during Case 3 at selected stations. (b) Time evolution of the variance wave spectrum at the Virginia deployment from measurements, stand-alone CFSR-driven WW3, baseline WRF-driven WW3, and two-way nested WW3, shown from left to right. Wave frequency (Hz) shown in the radial direction, and all times are UTC.

TABLE 7. As in Table 5, but for Case 3 (25 Mar 2016).

		Significant wave height (m)								Mean wave period (s)					
		RMSE			Bias		APE			RMSE			Bias		APE	
Station	N	Stand-alone	One-way	Two-way	Stand-alone	One-way	Two-way	Stand-alone	One-way	Stand-alone	One-way	Two-way	Stand-alone	One-way	Stand-alone	One-way	Two-way
44065	35	0.29	0.29	0.23	0.26	0.25	0.14	23.3	23.6	16.4	0.51	0.57	0.68	0.00	−0.19	−0.29	0.9	2.7	4.5
44025	35	0.53	0.39	0.31	0.49	0.36	0.22	33.4	26.7	18.6	0.43	0.50	0.61	0.11	0	−0.11	2.9	0.9	0.9
NJ	177	0.14	0.17	0.17	−0.02	−0.06	−0.10	2.1	5.2	6.8	0.85	0.74	0.81	0.57	0.50	0.32	15.6	13.7	10.0
44009	35	0.31	0.26	0.18	0.23	0.20	0.07	15.4	13.6	5.4	0.32	0.36	0.48	−0.16	−0.14	−0.22	2.6	2.2	3.8
44096	69	0.15	0.13	0.15	−0.04	−0.03	−0.10	2.9	2.1	8.7	0.74	0.69	0.78	−0.63	−0.61	−0.68	12.6	12.1	13.6
44099	70	0.15	0.13	0.15	−0.01	−0.01	−0.10	0.7	0.6	7.8	0.68	0.77	0.82	−0.55	−0.66	−0.71	10.6	12.6	13.6
44093	70	0.21	0.16	0.21	−0.02	−0.04	−0.16	0.3	2.3	9.5	0.70	0.78	0.81	−0.58	−0.66	−0.70	10.4	12.0	12.7
VA	177	0.19	0.16	0.14	0.03	0.05	−0.06	2.5	4.9	3.6	0.44	0.37	0.45	0.20	−0.08	−0.02	4.9	1.1	0.5
44014	35	0.28	0.22	0.13	0.19	0.14	−0.02	10.4	7.7	0.6	0.30	0.37	0.39	−0.20	−0.27	−0.31	3.6	4.9	5.6
44100	70	0.23	0.22	0.22	0.00	0.03	−0.07	1.8	3.8	3.4	0.90	0.95	0.97	−0.72	−0.77	−0.80	12.8	13.8	14.5
44095	68	0.11	0.11	0.18	0.02	−0.02	−0.13	1.4	0.20	6.3	0.43	0.44	0.45	−0.33	−0.32	−0.33	5.9	5.8	6.0
41025	35	0.53	0.46	0.35	0.45	0.38	0.27	24.0	20.3	14.5	0.39	0.32	0.33	−0.08	0	0.07	1.2	0.1	1.5

combined with two-way atmosphere/wave coupling, can lead tangible improvements in offshore hub-height wind speed predictions across a variety of forecast scenarios. How these results generalize to alternative locations, however, is not clear. An ongoing redeployment of the lidar buoys to the U.S. West Coast may help to answer this question. In addition, a more extensive set of representative cases would be helpful in order to increase the statistical robustness of our results.

Acknowledgments. This project was funded by the Wind Energy Technologies Office of the U.S. Department of Energy's Office of Energy Efficiency and Renewable Energy, under the management of Shannon Davis, Mike Derby, and Nate McKenzie. PNNL is operated by Battelle Memorial Institute for the U.S. Department of Energy under Contract DE-AC05-76RL01830. We also acknowledge the support and leadership of Alicia Mahon, the PNNL Lidar Buoy Program Manager.

Data availability statement. All data collected from the lidar buoys are publicly available at http://a2e.energy.gov/projects/buoy.

APPENDIX

Statistical Measure Formulas

In the following formulas M_i refers to each model value for output times $i = 1$ to N, while the corresponding observation is given by O_i:

$$\text{BIAS} = B \equiv \overline{M} - \overline{O} \equiv \sum_{i=1}^{N} M_i - \sum_{i=1}^{N} O_i,$$

$$\text{RMSE} \equiv \sqrt{\sum_{i=1}^{N} (M_i - O_i)^2},$$

$$\text{CRMSE} \equiv \sqrt{\sum_{i=1}^{N} (M_i - O_i - B)^2},$$

$$\text{corr} \equiv \frac{\sum_{i=1}^{N} (M_i - \overline{M})(O_i - \overline{O})}{\sqrt{\sum_{i=1}^{N} (M_i - \overline{M})^2 \sum_{i}^{N} (O_i - \overline{O})^2}}.$$

Finally, for the wave statistical tables we use absolute percent error (APE):

$$\text{APE} \equiv \left| \sum_{i=1}^{N} \frac{M_i - O_i}{O_i} \right|.$$

REFERENCES

Alves, J. M. R., A. Peliz, R. M. A. Caldeira, and P. M. A. Miranda, 2018: Atmosphere-ocean feedbacks in a coastal

upwelling system. *Ocean Modell.*, **123**, 55–65, https://doi.org/10.1016/j.ocemod.2018.01.004.

Archer, C. L., H. P. Simão, W. Kempton, W. B. Powell, and M. J. Dvorak, 2017: The challenge of integrating offshore wind power in the U.S. electric grid. Part I: Wind forecast error. *Renew. Energy*, **103**, 346–360, https://doi.org/10.1016/j.renene.2016.11.047.

Ardhuin, F., and Coauthors, 2010: Semiempirical dissipation source functions for ocean waves. Part I: Definition, calibration, and validation. *J. Phys. Oceanogr.*, **40**, 1917–1941, https://doi.org/10.1175/2010JPO4324.1.

——, S. T. Gille, D. Menemenlis, C. B. Rocha, N. Rascle, B. Chapron, J. Gula, and J. Molemaker, 2017: Small-scale open ocean currents have large effects on wind wave heights. *J. Geophys. Res. Oceans*, **122**, 4500–4517, https://doi.org/10.1002/2016JC012413.

Badger, M., A. Peña, A. N. Hahmann, A. A. Mouche, and C. B. Hasager, 2016: Extrapolating satellite winds to turbine operating heights. *J. Appl. Meteor. Climatol.*, **55**, 975–991, https://doi.org/10.1175/JAMC-D-15-0197.1.

Battjes, J. A., and J. P. F. M. Janssen, 1978: Energy loss and set-up due to breaking of random waves. *16th Int. Conf. on Coastal Engineering*, Hamburg, Germany, ASCE, 569–87.

Beljaars, A. C. M., and A. A. M. Holtslag, 1991: Flux parameterization over land surfaces for atmospheric models. *J. Appl. Meteor.*, **30**, 327–341, https://doi.org/10.1175/1520-0450(1991)030<0327:FPOLSF>2.0.CO;2.

Benjamin, S. G., and Coauthors, 2016: A North American hourly assimilation and model forecast cycle: The Rapid Refresh. *Mon. Wea. Rev.*, **144**, 1669–1694, https://doi.org/10.1175/MWR-D-15-0242.1.

Businger, J. A., J. C. Wyngaard, Y. Izumi, and E. F. Bradley, 1971: Flux–profile relationships in the atmospheric surface layer. *J. Atmos. Sci.*, **28**, 181–189, https://doi.org/10.1175/1520-0469(1971)028<0181:FPRITA>2.0.CO;2.

Carniel, S., A. Benetazzo, D. Bonaldo, F. M. Falcieri, M. M. Miglietta, A. Ricchi, and M. Sclavo, 2016: Scratching beneath the surface while coupling atmosphere, ocean and waves: Analysis of a dense water formation event. *Ocean Modell.*, **101**, 101–112, https://doi.org/10.1016/j.ocemod.2016.03.007.

Cavaleri, L., and P. Malanotte-Rizzoli, 1981: Wind wave prediction in shallow water: Theory and applications. *J. Geophys. Res.*, **86**, 10 961–10 973, https://doi.org/10.1029/JC086iC11p10961.

Charnock, H., 1981: Wind stress on a water surface. *Quart. J. Roy. Meteor. Soc.*, **81**, 639–640, https://doi.org/10.1002/qj.49708135027.

Doubrawa, P., R. J. Barthelmie, S. C. Pryor, C. B. Hasager, M. Badger, and I. Karagali, 2015: Satellite winds as a tool for offshore wind resource assessment: The Great Lakes Wind Atlas. *Remote Sens. Environ.*, **168**, 349–359, https://doi.org/10.1016/j.rse.2015.07.008.

Drennan, W. M., P. K. Taylor, and M. J. Yelland, 2005: Parameterizing the sea surface roughness. *J. Phys. Oceanogr.*, **35**, 835–848, https://doi.org/10.1175/JPO2704.1.

Edson, J. B., and C. W. Fairall, 1998: Similarity relationships in the marine atmospheric surface layer for terms in the TKE and scalar variance budgets. *J. Atmos. Sci.*, **55**, 2311–2328, https://doi.org/10.1175/1520-0469(1998)055<2311:SRITMA>2.0.CO;2.

——, and Coauthors, 2013: On the exchange of momentum over the open ocean. *J. Phys. Oceanogr.*, **43**, 1589–1610, https://doi.org/10.1175/JPO-D-12-0173.1.

Fairall, C. W., E. F. Bradley, J. E. Hare, A. A. Grachev, and J. B. Edson, 2003: Bulk parameterization of air–sea fluxes: Updates and verification for the COARE algorithm. *J. Climate*, **16**, 571–591, https://doi.org/10.1175/1520-0442(2003)016<0571:BPOASF>2.0.CO;2.

García Medina, G., W. J. Shaw, Z. Yang, and R. K. Newsom, 2020: Mid-Atlantic Bight wave hindcast to support DOE lidar buoy deployments: Model validation. Tech. Rep. PNNL-29814, PNNL, https://doi.org/10.2172/1635751.

Gelaro, R., and Coauthors, 2017: The Modern-Era Retrospective Analysis for Research and Applications, version 2 (MERRA-2). *J. Climate*, **30**, 5419–5454, https://doi.org/10.1175/JCLI-D-16-0758.1.

Grachev, A. A., C. W. Fairall, and E. F. Bradley, 2000: Convective profile constants revisited. *Bound.-Layer Meteor.*, **94**, 495–515, https://doi.org/10.1023/A:1002452529672.

Halliwell, G. R., 2004: Evaluation of vertical coordinate and vertical mixing algorithms in the HYbrid-Coordinate Ocean Model (HYCOM). *Ocean Modell.*, **7**, 285–322, https://doi.org/10.1016/j.ocemod.2003.10.002.

Hasager, C. B., and Coauthors, 2015: Offshore wind climatology based on synergetic use of Envisat ASAR, ASCAT and QuikSCAT. *Remote Sens. Environ.*, **156**, 247–263, https://doi.org/10.1016/j.rse.2014.09.030.

——, A. N. Hahmann, T. Ahsbahs, I. Karagali, T. Sile, M. Badger, and J. Mann, 2020: Europe's offshore winds assessed with synthetic aperture radar, ASCAT and WRF. *Wind Energy Sci.*, **5**, 375–390, https://doi.org/10.5194/wes-5-375-2020.

Hasselmann, K., and Coauthors, 1973: Measurements of wind-wave growth and swell decay during the Joint North Sea Wave Project (JONSWAP). *Ergaenzung. Z. Dtsch. Hydrogr. Z. A*, **12**, 1–95.

Hasselmann, S., K. Hasselmann, J. H. Allender, and T. P. Barnett, 1985: Computations and parameterizations of the nonlinear energy transfer in a gravity-wave spectrum. Part II: Parameterizations of the nonlinear energy transfer for application in wave models. *J. Phys. Oceanogr.*, **15**, 1378–1391, https://doi.org/10.1175/1520-0485(1985)015<1378:CAPOTN>2.0.CO;2.

Hersbach, H., and Coauthors, 2020: The ERA5 global reanalysis. *Quart. J. Roy. Meteor. Soc.*, **146**, 1999–2049, https://doi.org/10.1002/qj.3803.

Jiménez, P. A., and J. Dudhia, 2018: On the need to modify the sea surface roughness formulation over shallow waters. *J. Appl. Meteor. Climatol.*, **57**, 1101–1110, https://doi.org/10.1175/JAMC-D-17-0137.1.

Jones, P. W., 1998: A user's guide for SCRIP: A Spherical Coordinate Remapping and Interpolation Package, v1.4. Los Alamos National Laboratory, 27 pp.

Karagali, I., A. N. Hahmann, M. Badger, C. Hasager, and J. Mann, 2018: New European wind atlas offshore. *J. Phys.: Conf. Ser.*, **1037**, 052007, https://doi:10.1088/1742-6596/1037/5/052007.

Lundquist, J. K., and Coauthors, 2017: Assessing state-of-the-art capabilities for probing the atmospheric boundary layer: The XPIA field campaign. *Bull. Amer. Meteor. Soc.*, **98**, 289–314, https://doi.org/10.1175/BAMS-D-15-00151.1.

Nelson, J., and R. He, 2012: Effect of the Gulf Stream on winter extratropical cyclone outbreaks. *Atmos. Sci. Lett.*, **13**, 311–316, https://doi.org/10.1002/asl.400.

——, ——, J. C. Warner, and J. Bane, 2014: Air-sea interactions during strong winter extratropical storms. *Ocean Dyn.*, **64**, 1233–1246, https://doi.org/10.1007/s10236-014-0745-2.

Newsom, R. K., 2016: Optimizing lidar wind measurements from the DOE WindSentinel Buoys. Pacific Northwest National Laboratory Rep. PNNL-25512, 36 pp., PNNL, https://www.

pnnl.gov/main/publications/external/technical_reports/PNNL-25512.pdf.

——, L. M. Sheridan, B. J. Gaudet, G. G. Medina, Z. Yang, R. Krishnamurthy, and W. J. Shaw, 2020: A study on modeled wind speed errors using the U.S. Department of Energy buoys. Pacific Northwest National Laboratory Rep. PNNL-30117, 62 pp., PNNL, https://doi.org/10.2172/1713065.

Olabarrieta, M., J. C. Warner, and B. Armstrong, 2012: Ocean–atmosphere dynamics during Hurricane Ida and Nor'Ida: An application of the Coupled Ocean–Atmosphere–Wave–Sediment Transport (COAWST) modeling system. *Ocean Modell.*, **43–44**, 112–137, https://doi.org/10.1016/j.ocemod.2011.12.008.

Oost, W., G. J. Komen, C. M. J. Jacobs, and C. Van Oort, 2002: New evidence for a relation between wind stress and wave age from measurements during ASGAMAGE. *Bound.-Layer Meteor.*, **103**, 409–438, https://doi.org/10.1023/A:1014913624535.

Ren, D., J. Du, F. Hua, Y. Yang, and L. Han, 2016: Analysis of different atmospheric physical parameterizations in COAWST modeling system for the Tropical Storm Nock-ten application. *Nat. Hazards*, **82**, 903–920, https://doi.org/10.1007/s11069-016-2225-0.

Renault, L., J. Chiggiato, J. C. Warner, M. Gomez, G. Vizoso, and J. Tintoré, 2012: Coupled atmosphere–ocean–wave simulations of a storm event over the Gulf of Lion and Balearic Sea. *J. Geophys. Res.*, **117**, C09019, https://doi.org/10.1029/2012JC007924.

Ricchi, A., M. Miglietta, P. Falco, A. Benetazzo, D. Bonaldo, A. Bergamasco, M. Sclavo, and S. Carniel, 2016: On the use of a coupled ocean–atmosphere–wave model during an extreme cold air outbreak over the Adriatic Sea. *Atmos. Res.*, **172–173**, 48–65, https://doi.org/10.1016/j.atmosres.2015.12.023.

——, and Coauthors, 2017: Sensitivity of a Mediterranean tropical-like cyclone to different model configurations and coupling strategies. *Atmosphere*, **8**, 92, https://doi.org/10.3390/atmos8050092.

Saha, S., and Coauthors, 2010: The NCEP Climate Forecast System Reanalysis. *Bull. Amer. Meteor. Soc.*, **91**, 1015–1057, https://doi.org/10.1175/2010BAMS3001.1.

——, and Coauthors, 2014: The NCEP Climate Forecast System version 2. *J. Climate*, **27**, 2185–2208, https://doi.org/10.1175/JCLI-D-12-00823.1.

Shaw, W. J., and Coauthors, 2020: General analysis of data collected from DOE lidar buoy deployments off Virginia and New Jersey. Pacific Northwest National Laboratory Rep. PNNL-29823, PNNL, https://doi.org/10.2172/1632348.

Sheridan, L. M., R. Krishnamurthy, A. M. Gorton, W. J. Shaw, and R. K. Newsom, 2020: Validation of reanalysis-based offshore wind resource characterization using lidar buoy observations. *Mar. Technol. Soc. J.*, **54**, 44–61, https://doi.org/10.4031/MTSJ.54.6.13.

——, ——, and B. J. Gaudet, 2021: Assessment of model hub height wind speed performance using DOE lidar buoy data. Pacific Northwest National Laboratory PNNL-30840, PNNL, https://www.pnnl.gov/publications/assessment-model-hub-height-wind-speed-performance-using-doe-lidar-buoy-data.

Skamarock, W. C., and Coauthors, 2019: A description of the Advanced Research WRF Model version 4. NCAR Tech. Note NCAR/TN-556+STR, 145 pp., https://doi.org/10.5065/1dfh-6p97.

Stauffer, D. R., and N. L. Seaman, 1994: Multiscale four-dimensional data assimilation. *J. Appl. Meteor.*, **33**, 416–434, https://doi.org/10.1175/1520-0450(1994)033<0416:MFDDA>2.0.CO;2.

Taylor, P. K., and M. A. Yelland, 2001: The dependence of sea surface roughness on the height and steepness of the waves. *J. Phys. Oceanogr.*, **31**, 572–590, https://doi.org/10.1175/1520-0485(2001)031<0572:TDOSSR>2.0.CO;2.

The WAVEWATCH III Development Group, 2016: User manual and system documentation of WAVEWATCH III version 5.16. Tech. Note 329, NOAA/NWS/NCEP/MMAB, 361 pp., https://polar.ncep.noaa.gov/waves/wavewatch/manual.v5.16.pdf.

Warner, J. C., B. Armstrong, R. He, and J. B. Zambon, 2010: Development of a Coupled Ocean-Atmosphere-Wave-Sediment Transport (COAWST) modeling system. *Ocean Modell.*, **35**, 230–244, https://doi.org/10.1016/j.ocemod.2010.07.010.

Zambon, J. B., R. He, and J. C. Warner, 2014a: Tropical to extratropical: Marine environmental changes associated with Superstorm Sandy prior to its landfall. *Geophys. Res. Lett.*, **41**, 8935–8943, https://doi.org/10.1002/2014GL061357.

——, ——, and ——, 2014b: Investigation of Hurricane Ivan using the Coupled Ocean-Atmosphere-Wave-Sediment Transport (COAWST) model. *Ocean Dyn.*, **64**, 1535–1554, https://doi.org/10.1007/s10236-014-0777-7.

Zang, Z., G. Xue, S. Bao, Q. Chen, N. D. Walker, A. S. Haag, Q. Ge, and Z. Yao, 2018: Numerical study of sediment dynamics during Hurricane Gustav. *Ocean Modell.*, **126**, 29–42, https://doi.org/10.1016/j.ocemod.2018.04.002.

Zhao, X., and J. C. L. Chan, 2017: Effect of the initial vortex size on intensity change in the WRF-ROMS coupled model. *J. Geophys. Res. Oceans*, **122**, 9636–9648, https://doi.org/10.1002/2017JC013283.